

KERNEL SMOOTHING OPERATORS ON THICK OPEN DOMAINS*

DIMITRIOS GIANNAKIS[†] AND MOHAMMAD JAVAD LATIFI JEBELLI[‡]

Abstract. We define the notion of a thick open set Ω in a Euclidean space and show that a local Hardy-Littlewood inequality holds in $L^p(\Omega)$, $p \in (1, \infty]$. We then establish pointwise and $L^p(\Omega)$ convergence for families of convolution operators with a Markov normalization on Ω . We demonstrate application of such smoothing operators to piecewise-continuous density, velocity, and stress fields from discrete element models of sea ice dynamics.

Key words. Convolution operators, kernel integral operators, Hardy-Littlewood inequality, approximation of the identity, discrete element models, sea ice

MSC codes. 42B25 , 62G07 , 44A35

1. Introduction. Let $h \in L^1(\mathbb{R}^n)$ be a non-negative, radially symmetric function with $\int_{\mathbb{R}^n} h(x) dx = 1$, and let $h_\epsilon(x) = \epsilon^{-n} h(x/\epsilon)$ for $\epsilon > 0$. The Hardy-Littlewood maximal operator of convolution type, M_h , is defined as

$$(1.1) \quad M_h f(x) = \sup_{\epsilon > 0} |h_\epsilon * f(x)|,$$

where $f \in L^p(\mathbb{R}^n)$ with $p > 1$. The Hardy-Littlewood maximal inequality,

$$\|M_h f\|_{L^p(\mathbb{R}^n)} \leq A \|f\|_{L^p(\mathbb{R}^n)}, \quad A > 0,$$

can be employed to prove pointwise and L^p convergence of $h_\epsilon * f$ to f as $\epsilon \rightarrow 0$. Results of this type find applications in many areas, including function approximation, analysis of partial differential equations (PDEs), and harmonic analysis.

The theory of Hardy-Littlewood maximal functions has been studied and generalized intensively over the past decades; see e.g., Stein [46]. Examples include maximal operators on the Sobolev spaces $W^{1,p}(\mathbb{R}^n)$, where associated boundedness results are employed in PDE regularity theory [29, 20, 33, 44, 18, 6, 5]. A more general definition of the maximal operator in the context of a metric measure space (X, d, μ) is given by

$$Mf(x) = \sup_{\epsilon > 0} \frac{1}{\mu(B_\epsilon(x))} \int_{B_\epsilon(x)} f d\mu$$

where $B_\epsilon(x) = \{y \in X : d(x, y) < \epsilon\}$. For recent developments in this area, see [51, 17, 34, 47, 48]. A further generalization of the theory is to consider fractional maximal functions,

$$M^\alpha f(x) = \sup_{\epsilon > 0} \frac{\epsilon^\alpha}{\mu(B_\epsilon(x))} \int_{B_\epsilon(x)} f d\mu, \quad \alpha > 0,$$

which also have applications in analysis and PDE; e.g., [1]. In the context of weighted L^p spaces, a fundamental question is to identify weight functions $w(x)$ such that the maximal operator is bounded on $L^p(\mathbb{R}^n, w(x) dx)$ [50].

*Submitted to the editors DATE.

Funding: The authors acknowledge support from ONR MURI N00014-19-1-242.

[†]Department of Mathematics, Dartmouth College, Hanover, NH (dimitrios.giannakis@dartmouth.edu).

[‡]Department of Mathematics, Dartmouth College, Hanover, NH (mohammad.javad.latifi.jebelli@dartmouth.edu).

Another variant of the basic definition (1.1) is to consider so-called local maximal operators of the form

$$M_h f(x) = \sup_{0 < \epsilon < \epsilon_0} |h_\epsilon * f(x)|$$

for some $\epsilon_0 > 0$. Here, the term “local” refers to the fact that the supremum is taken locally over $\epsilon \in (0, \epsilon_0)$. See [30, 50, 14, 38, 40] for further details on local maximal functions.

1.1. Our contributions. In this paper, we consider an open domain $\Omega \subset \mathbb{R}^n$ as a metric measure space with the metric and measure structures inherited from those of \mathbb{R}^n . In this case, the local maximal operator becomes

$$(1.2) \quad \tilde{M}f(x) = \sup_{0 < \epsilon < \epsilon_0} \frac{1}{\mu(\Omega \cap B_\epsilon(x))} \int_{\Omega \cap B_\epsilon(x)} f d\mu.$$

Here, as a generalization of (1.2), we consider convolution-type local maximal operators of the form

$$\tilde{M}_h f(x) = \sup_{0 < \epsilon < \epsilon_0} \left| \frac{h_\epsilon * f(x)}{h_\epsilon * 1_\Omega(x)} \right|,$$

with 1_Ω being the characteristic function of the set Ω . Building upon a “thickness” condition for Ω , which is related to a local doubling property of metric measure spaces (but is independent from the global notion of doubling), we establish the counterpart of the Hardy–Littlewood maximal inequality for \tilde{M}_h . In our main result, Theorem 2.8, we use this inequality to prove convergence of $P_\epsilon f$ to f pointwise and in $L^p(\Omega)$ norm, where P_ϵ denotes the normalized smoothing operator given by

$$P_\epsilon f = \frac{h_\epsilon * f}{h_\epsilon * 1_\Omega}.$$

Furthermore, we establish $L^p(\Omega)$ norm convergence results for variants of P_ϵ associated with bistochastic kernels using ideas from [9, 13] (see Theorem 5.1). A benefit of smoothing with P_ϵ rather than the raw convolution operator $f \mapsto h_\epsilon * f$ is that the former preserves constant functions on Ω , whereas the latter does not. In the bistochastic case, P_ϵ additionally preserves integrals of functions; i.e., smoothing is mass-preserving. Aspects of numerical approximation of these operators using triangulation and numerical quadrature over polygonal domains are also studied in this paper.

As an application of our approach, we perform smoothing of piecewise-continuous density, velocity, and stress fields generated by discrete element models (DEMs) of sea ice dynamics over geometrically complex domains. In the following subsection, we outline elements of sea ice dynamics and its representation within DEMs that motivate this application.

1.2. Motivation: Sea Ice Dynamics. Sea ice is a critical component of the Earth’s climate system. Existing at the interface between the atmosphere and the ocean, it regulates the turbulent transfer of heat, moisture, and momentum between the two media while also drastically affecting radiative heat fluxes via the ice-albedo effect. As a physical medium, sea ice exhibits a highly multiscale nature [16]. In regions of relatively low concentration, sea ice cover consists of ice floes (discrete floating chunks of ice) of size $O(10 \text{ m})$ to $O(100 \text{ km})$ that move under atmospheric and oceanic drag, undergoing a variety of dynamic and thermodynamic processes such as collisions, fracture, ridging, melt and growth. On larger scales, $O(100 \text{ km})$

to $O(1000 \text{ km})$, the emergent macro-scale behavior is that of a fluid with a highly nonlinear, complex rheology that exhibits aspects of viscous/creep flow for low stress and plastic deformation at sufficiently high stress [25, 27, 12]. This complex rheology manifests in the formation of intricate networks of narrow failure zones, known as linear kinematic features (LKFs), that can span several hundred kilometers in length while being as narrow as a few tenths of meters [32].

Most current-generation sea ice models treat sea ice as a continuum, using PDE solvers to solve the mass and momentum balance equations along with equations for thermodynamics. These models have been reasonably successful in simulating large-scale aspects of sea ice dynamics, such as thickness, concentration, and velocity [31]. With the increase of computational capabilities over the years, and aided by the development of efficient solvers [45], continuum models have also been able to successfully simulate aspects of LKFs [28], even down to kilometer-scale resolution [53]. Yet, it is widely accepted that at lengthscales approaching the floe scale, and particularly in regions of low ice concentration, the continuum hypothesis eventually breaks down [10, 24].

Discrete element models (DEMs) offer an alternative approach to sea ice modeling that is well-suited to overcome some of the known biases and limitations of continuum models [3]. Unlike continuum models, DEMs treat sea ice as a granular medium consisting of Lagrangian objects that represent ice floes. Early efforts to discrete element modeling of sea ice date back at least to the mid 1990s [26]. Since then, a variety of techniques have been developed that represent ice floes as disks undergoing collisions [11], collections of bonded grains of fixed [22, 52] or arbitrary [39, 37] shapes, and interacting polygons [35], among other approaches. Promising results obtained with sea ice DEMs include simulation of arching in the Nares Strait [52], reproduction of realistic floe-size distributions in winter (high ice concentration) configurations [35], and modeling of quasi-three-dimensional processes such as wave-induced fracture [23]. Besides geophysical applications, DEMs of sea ice have also been employed in engineering applications such as simulation of ice–structure interactions [49].

DEMs present unique challenges when it comes to postprocessing and integration of these models within larger weather and climate models. First, sea ice exhibits highly nonlinear dynamical coupling with the ocean and atmosphere, whose properties influence considerably the nature of upper-ocean turbulence and heat and momentum fluxes between the ocean and atmosphere [19, 36, 54]. Given that most atmospheric and oceanic models are based on Eulerian representations of the respective dynamic and thermodynamic fields, the Lagrangian/granular nature of sea ice DEMs complicates this coupling and imposition of boundary conditions, particularly with regards to representation of sharp edges and discontinuities in DEM output. Similar issues are faced by data assimilation systems that have to contend with Lagrangian observations of sea ice floes in order to estimate the state of the underlying ocean circulation [7]. Collectively, these challenges motivate the development of smoothing schemes that can produce continuous approximations of DEM variables with well-characterized convergence properties. The ability to extract Eulerian/continuum information from DEM output can also aid the development of improved macro-scale rheologies for sea ice, which would in turn lead to improvement of large-scale continuum sea ice models.

Here, as an application of our kernel smoothing framework, we analyze data from a simulation of densely packed ice floes under compression and a Nares Strait simulation conducted using the recently developed SubZero DEM [35]. We focus on smooth approximations of the mass density, ice velocity, and stress tensor fields obtained by the Markovian integral operators P_ϵ . Applying these operators to piecewise-continuous

fields from DEM snapshots yields continuous fields whose smoothness is controlled by the choice of kernel. The compression experiments capture the ice velocity and stress patterns associated with the formation of idealized LKFs in the simulation. Meanwhile, the Nares Strait experiments reveal buildup and release of stress, and associated intermittent ice motion, induced by jamming and fracture of ice floes passing through the Nares Strait.

1.3. Organization of the paper. Section 2 describes our approach for smoothing with Markov-normalized integral operators on thick domains. Section 3 contains an analysis of the pointwise and L^p norm convergence of these operators. Section 4 examines the relation between thickness and doubling of metric measure spaces. Section 5 studies the case of Markov integral operators with bistochastic kernels. In section 6, we discuss aspects of numerical approximation over polygonal domains. Section 7 describes our analyses of sea ice DEM simulation data. Section 8 contains a summary discussion and our primary conclusions. Proofs of certain auxiliary results are included in Appendix A. A Python implementation of the kernel smoothing methods described in this paper can be found in the repository <https://github.com/SeaIce-Math/KSPoly>.

2. Kernel smoothing on thick domains. Let Ω be an open subset of \mathbb{R}^n . We consider the problem of approximating measurable functions $f : \Omega \rightarrow \mathbb{R}$ using kernel operators conditioned on Ω .

2.1. Notation. For a Banach space E , $B(E)$ will denote the Banach space of bounded linear operators on E , equipped with the operator norm. Given a Lebesgue-measurable set $X \subseteq \mathbb{R}^n$, $L(X)$ will denote the space of Lebesgue-measurable real-valued functions on X , and $L^p(X)$ with $1 \leq p \leq \infty$ will denote the standard L^p spaces on X equipped with the norms $\|f\|_{L^p(X)} = (\int_X |f(x)|^p dx)^{1/p}$ for $1 \leq p < \infty$ and $\|f\|_{L^\infty(X)} = \text{ess sup}_{x \in X} |f(x)|$. Moreover, $C(X)$ will be the space of continuous real-valued functions on X , and $C_c(X)$, $C_b(X)$ the subspaces of $C(X)$ consisting of compactly supported and bounded functions, respectively. We equip $C_c(X)$ and $C_b(X)$ with the uniform norm, $\|f\|_\infty = \sup_{x \in X} |f(x)|$. If X is open, $C^r(X)$ will be the space of r -times continuously differentiable functions on that set. Given a subset $X \subseteq \mathbb{R}^n$, \bar{X} will denote its closure and $1_X : \mathbb{R}^n \rightarrow \mathbb{R}$ will be the characteristic function of that set. For $x \in \mathbb{R}^n$, $T_x : L(\mathbb{R}^n) \rightarrow L(\mathbb{R}^n)$ will denote the translation operator $T_x f(y) = f(y - x)$. Moreover, $\check{\cdot} : L(X) \rightarrow L(X)$ will be the ‘‘flip’’ operator, $f^\check{\cdot}(x) = f(-x)$, and $f_1 * f_2(x) = \int_{\mathbb{R}^n} f_1(x - y) f_2(y) dy$ the convolution of $f_1, f_2 \in L(\mathbb{R})$ (whenever that operation is well-defined). We let $\mathcal{F} : L^2(\mathbb{R}^n) \rightarrow \mathbb{R}^n$ denote the unitary Fourier operator on $L^2(\mathbb{R}^n)$, defined by extension of $\mathcal{F}f = \int_{\mathbb{R}^n} e^{-i\omega \cdot x} f(x) dx$ for $f \in C_c(\mathbb{R}^n)$. We shall denote the Euclidean norm of a vector $x \in \mathbb{R}^n$ as $\|x\|$. For $r \geq 0$ we define $\hat{H}^r(\mathbb{R}^n) \subseteq L^2(\mathbb{R}^n)$ as the closure of $C_c(\mathbb{R}^n)$ with respect to the norm $\|\hat{f}\|_{H^r(\mathbb{R}^n)} = (\int_{\mathbb{R}^n} |\hat{f}(\omega)|^2 (1 + \|\omega\|^2)^r d\omega)^{1/2}$ and $H^r(\mathbb{R}^n) = \mathcal{F}^* \hat{H}^r(\mathbb{R}^n)$ as the inverse Fourier image of $\hat{H}^r(\mathbb{R}^n)$. For $r \in \mathbb{N}_0$, $H^r(\mathbb{R}^n)$ is isomorphic to the Sobolev subspace of $L^2(\mathbb{R}^n)$ of order r defined in terms of weak derivatives.

2.2. Radial kernels and associated integral operators. The starting point of our construction is a positive, radially symmetric, normalized function $h \in L^1(\mathbb{R}^n)$. Specifically, we require:

- (K1) $h(x) \geq 0$ for every $x \in \mathbb{R}^n$.
- (K2) $h(Ox) = h(x)$ for every $x \in \mathbb{R}^n$ and orthogonal matrix $O \in \mathbb{R}^{n \times n}$.
- (K3) $\|h\|_{L^1(\mathbb{R}^n)} = 1$.

In some cases, we will additionally require:

(K4) h is radially decreasing; that is, $h(y) \leq h(x)$ for every $x, y \in \mathbb{R}^n$ such that $\|x\| \leq \|y\|$.

A concrete example of a function having all of Properties (K1)–(K4) (which we will use in the numerical experiments of section 7) is the Gaussian radial basis function (RBF),

$$(2.1) \quad h(x) = \frac{1}{(2\pi)^{n/2}} e^{-\|x\|^2/2}.$$

To any h satisfying Properties (K1)–(K3), we associate a one-parameter family of functions $h_\epsilon : \mathbb{R}^n \rightarrow \mathbb{R}$ and corresponding kernels $k_\epsilon : \mathbb{R}^n \times \mathbb{R}^n \rightarrow \mathbb{R}$, where

$$(2.2) \quad h_\epsilon(x) = \epsilon^{-n} h(x/\epsilon), \quad k_\epsilon(x, y) = h_\epsilon(y - x).$$

In what follows, we will refer to kernels k_ϵ obtained in this manner as *radial kernels* and the underlying function h as *shape function*. Note that every radial kernel is translation-invariant and symmetric, i.e.,

$$k_\epsilon(x + z, y + z) = k_\epsilon(x, y), \quad k_\epsilon(x, y) = k_\epsilon(y, x),$$

respectively, for all $x, y, z \in \mathbb{R}^n$.

Every radial kernel k_ϵ induces an integral operator $K_\epsilon : L^1(\mathbb{R}^n) \rightarrow L^1(\mathbb{R}^n)$ that acts on functions by convolution,

$$(2.3) \quad K_\epsilon f := \int_{\mathbb{R}^n} k_\epsilon(\cdot, y) f(y) dy \equiv h_\epsilon * f.$$

In particular, since $\|h_\epsilon * f\|_{L^1(\mathbb{R}^n)} \leq \|h_\epsilon\|_{L^1(\mathbb{R}^n)} \|f\|_{L^1(\mathbb{R}^n)}$ and $\|h_\epsilon\|_{L^1(\mathbb{R}^n)} = \|h\|_{L^1(\mathbb{R}^n)} = 1$, K_ϵ is a contraction on $L^1(\mathbb{R}^n)$, ■

$$(2.4) \quad \|K_\epsilon f\|_{L^1(\mathbb{R}^n)} \leq \|f\|_{L^1(\mathbb{R}^n)}.$$

We will continue to use the symbol K_ϵ to denote integral operators acting on function spaces other than $L^1(\mathbb{R}^n)$ via the formula (2.3).

Next, we state some basic results on the regularity of functions in the range of K_ϵ .

LEMMA 2.1. *Set $p \in (1, \infty]$ and $q \in [1, \infty)$ with $\frac{1}{p} + \frac{1}{q} = 1$. Then, for every $h \in L^q(\mathbb{R}^n)$ and $f \in L^p(\mathbb{R}^n)$, the function $K_\epsilon f$ is continuous and bounded with $\|K_\epsilon f\|_\infty \leq \|h\|_{L^q(\mathbb{R}^n)} \|f\|_{L^p(\mathbb{R}^n)}$.*

Proof. See Appendix A. □

It follows by Lemma 2.1 that K_ϵ maps bounded measurable functions to continuous functions. Moreover, it can be shown that if $\Omega \subset \mathbb{R}^n$ is open and h is smooth and compactly supported, K_ϵ maps locally integrable functions to functions in $C^\infty(\Omega \setminus \Omega_\epsilon)$, where $\Omega_\epsilon = \{x \in \Omega : B_\epsilon(x) \not\subset \Omega\}$ (see, e.g., [15, Appendix C.4]).

LEMMA 2.2. *For every $h \in H^r(\mathbb{R}^n)$, $r \in \mathbb{N}_0$, and $f \in L^2(\mathbb{R}^n)$ the function $K_\epsilon f$ lies in $C^r(\mathbb{R}^n)$.*

Proof. See Appendix A. □

2.3. Smoothing with integral operators. Given a function $f \in L^1(\Omega)$, we view $K_\epsilon f$ from (2.3) as an approximation of f with regularity controlled by the kernel k_ϵ . Intuitively, as ϵ decreases, the locality of k_ϵ increases, and we expect $K_\epsilon f$ to converge to f in some sense. To illustrate this convergence with a concrete example, we recall the Lebesgue differentiation theorem. Let $B_\epsilon(x)$ be the open ball of radius ϵ centered at $x \in \mathbb{R}^n$ and $|B_\epsilon(x)|$ its Lebesgue measure. Let also $B \equiv B_1(0)$ be the unit ball centered at the origin. The Lebesgue differentiation theorem states that for every measurable function $f : \mathbb{R}^n \rightarrow \mathbb{R}$ the functions defined as

$$\tilde{g}_\epsilon(x) = \frac{1}{|B_\epsilon(x)|} \int_{B_\epsilon(x)} f(y) dy$$

for a.e. $x \in \mathbb{R}^n$ converge as $\epsilon \rightarrow 0^+$ to f a.e. One can rewrite the above expression in kernel form by defining

$$(2.5) \quad l(x) = \frac{1}{|B|} 1_B(x), \quad l_\epsilon(x) = \epsilon^{-n} 1_{B(x/\epsilon)}, \quad \tilde{k}_\epsilon(x, y) = l_\epsilon(y - x),$$

so that

$$\tilde{g}_\epsilon(x) = \int_{\mathbb{R}^n} \tilde{k}_\epsilon(x, y) f(y) dy \equiv l_\epsilon * f(x),$$

for a.e. $x \in \mathbb{R}^n$. As one can readily verify, l satisfies Properties (K1)–(K4), and thus we can interpret \tilde{g}_ϵ as a special case of (2.3) for the shape function set to the “tophat” function 1_B supported on the unit ball. In other words, the Lebesgue differentiation theorem provides an example of kernel-smoothed functions \tilde{g}_ϵ that pointwise-recover the input function f .

The a.e. convergence result for \tilde{g}_ϵ to f based on the Lebesgue differentiation theorem can be extended to general radial kernels using the theory of Hardy-Littlewood maximal functions. Given a shape function $h \in L^1(\mathbb{R}^n)$, the local Hardy-Littlewood maximal function associated with $f \in L^p(\mathbb{R}^n)$ is defined as

$$(2.6) \quad M_h f(x) = \sup_{\epsilon > 0} |h_\epsilon * f(x)|,$$

with h_ϵ defined in (2.2). The following theorems can be found in [46, pp. 23, 71].

THEOREM 2.3 (Local Hardy-Littlewood maximal inequality). *Suppose that $h \in L^1(\mathbb{R}^n)$ satisfies Properties (K1)–(K4). Then, for every $1 < p \leq \infty$ there exists $A > 0$ such that for every $f \in L^p(\mathbb{R}^n)$ the maximal function $M_h f$ satisfies*

$$\|M_h f\|_{L^p(\mathbb{R}^n)} \leq A \|f\|_{L^p(\mathbb{R}^n)}.$$

THEOREM 2.4. *Suppose that $h \in L^1(\mathbb{R}^n)$ satisfies Properties (K1)–(K4) and the decay bound $|h(x)| \leq C(1 + |x|)^{-n-\delta}$ for some $C, \delta > 0$. Then, for every $f \in L^p(\mathbb{R}^n)$ with $1 < p \leq \infty$, the family of functions $K_\epsilon f = h_\epsilon * f$ lies in $L^p(\mathbb{R}^n)$ and converges to f a.e. as $\epsilon \rightarrow 0^+$.*

By Theorem 2.4, we see that functions in $L^p(\mathbb{R}^n)$ with $1 < p \leq \infty$ can be pointwise approximated by smoothed functions using general radial kernels. Combining Theorems 2.3 and 2.4 yields:

COROLLARY 2.5. *With the assumptions and notation of Theorem 2.4, $K_\epsilon f$ converges to f in $L^p(\mathbb{R}^n)$ norm for every $p \in (1, \infty)$.*

Proof. The claim follows similarly to Claim 2 of Theorem 2.8, which is proved in subsection 3.3. \square

Despite these encouraging results, a shortcoming of smoothing using integral operators such as K_ϵ that are not adapted to the domain Ω is that, in general, if f is constant on Ω , $K_\epsilon f$ will not be a constant function on that domain. Moreover, if f and \tilde{g}_ϵ are integrable on Ω , the integrals $\int_\Omega f(x) dx$ and $\int_\Omega K_\epsilon f(x) dx$ will generally not be equal. Preservation of constant functions and integrals are important properties, particularly when dealing with observables of physical systems. In the following subsection, we describe a modified scheme that employs Markov-normalized versions of K_ϵ on domains satisfying a “thickness” condition to ensure preservation of constant functions and integrals, as well as pointwise and L^p norm convergence.

2.4. Thick domains and Markov normalization. Given a measurable set $\Omega \subseteq \mathbb{R}^n$, a measurable function $p : \Omega \times \Omega \rightarrow \mathbb{R}$ will be said to be a *Markov kernel* if (i) $p(x, y) \geq 0$; and (ii) $\int_\Omega p(x, s) ds = 1$ for all $x, y \in \Omega$. Every Markov kernel has the property that for a constant function $f : \Omega \rightarrow \mathbb{R}$, the function $g : \Omega \rightarrow \mathbb{R}$ with

$$(2.7) \quad g(x) = \int_\Omega p(x, y) f(y) dy$$

is also constant and equal to f . This suggests that smoothing operators associated with Markov kernels are good candidates for addressing the failure of smoothing using un-normalized kernels to preserve constant functions. We now describe a procedure to normalize a family of radial kernels $k_\epsilon : \mathbb{R}^n \times \mathbb{R}^n \rightarrow \mathbb{R}$ to a corresponding family of Markov kernels $p_\epsilon : \Omega \times \Omega \rightarrow \mathbb{R}$ such that the formula (2.7) leads to bounded integral operators on $L^p(\Omega)$ that preserve constant functions.

Our construction employs a notion of thickness of the domain Ω , which we now define.

DEFINITION 2.6 (Thick set). *A Lebesgue-measurable set $\Omega \subseteq \mathbb{R}^n$ is said to be thick if there exists $c, \epsilon_0 > 0$ such that for all $\epsilon \in (0, \epsilon_0)$ and $x \in \Omega$,*

$$|B_\epsilon(x) \cap \Omega| > c |B_\epsilon(x)|.$$

Note that the inequality in Definition 2.6 can be equivalently expressed as $l_\epsilon * 1_\Omega(x) > c$, where l_ϵ is the scaled tophat function from (2.5). By the Lebesgue differentiation theorem, the function

$$(2.8) \quad \rho_\Omega(x) = \lim_{\epsilon \rightarrow 0} \frac{|B_\epsilon(x) \cap \Omega|}{|B_\epsilon(x)|},$$

known as the *Lebesgue density function* of Ω , is well-defined for a.e. $x \in \mathbb{R}^n$. We can thus interpret thick sets as measurable subsets of \mathbb{R}^n with approximate Lebesgue densities bounded below. Examples of thick sets include polygons, solid spheres, and other domains commonly used in numerical applications; see subsection 3.1. More generally, for an interior point x of a measurable set $\Omega \subseteq \mathbb{R}^n$ and for small-enough ϵ we have $B_\epsilon(x) \subset \Omega$ —this implies that the limit in (2.8) exists and $\rho_\Omega(x) = 1$ for every interior point. However, for points in the boundary of Ω the Lebesgue density may not exist.

Given a shape function $h \in L^1(\mathbb{R}^n)$ and a Borel-measurable set $\Omega \subseteq \mathbb{R}^n$, we define for each $\epsilon > 0$ the function $d_\epsilon : \Omega \rightarrow \mathbb{R}$ as

$$(2.9) \quad d_\epsilon = K_\epsilon 1_\Omega \equiv h_\epsilon * 1_\Omega.$$

By Lemma 2.1, d_ϵ is continuous on \mathbb{R}^n and it is clearly positive. If, in addition, h is smooth and compactly supported, local integrability of 1_Ω implies that d_ϵ lies in $C^\infty(\Omega \setminus \Omega_\epsilon)$. We will refer to d_ϵ as a *degree function* by analogy with the notion of degree vectors associated with discrete kernel integral operators on graphs; e.g., [8].

The following proposition provides sufficient conditions for the strict positivity of d_ϵ that allow us to employ these functions them for Markov normalization.

PROPOSITION 2.7. *Let $h \in L^1(\mathbb{R}^n)$ be a shape function satisfying Properties (K1)–(K3), $\Omega \subseteq \mathbb{R}^n$ an open set, and d_ϵ the corresponding degree functions from (2.9).*

1. *If Ω is bounded, and in addition h satisfies Property (K4), then for every $\epsilon > 0$ there exists $c_\epsilon > 0$ such that for every $x \in \bar{\Omega}$ we have $d_\epsilon(x) \geq c_\epsilon$.*
2. *If Ω is thick, then there exists $c, \epsilon_0 > 0$ such that for every $\epsilon \in (0, \epsilon_0)$ and $x \in \bar{\Omega}$ we have $d_\epsilon(x) \geq c$.*

Proof. Claim 2 is proved as Lemma 3.1 in subsection 3.1.

To prove Claim 1, after a change of variables, it is enough to consider the case $x = 0$. We claim that if $0 \in \bar{\Omega}$ then

$$(2.10) \quad \int_{\Omega} h_\epsilon(x) dx > 0$$

for any $\epsilon > 0$. To prove this, take an arbitrary open ball B_ϵ of radius ϵ centered at the origin. Since $B_\epsilon \cap \Omega$ is open, we can find another ball $B \subset B_\epsilon \cap \Omega$. Assume, for contradiction, that $\int_{\Omega} h_\epsilon(x) dx = 0$. By Property (K1), this implies $\int_B h_\epsilon(x) dx = 0$, and thus $h(x) = 0$ for a.e. $x \in B$. Now let $A = \{Ox \in \mathbb{R}^n : O \in O(n), x \in B\}$ be the spherical shell generated by B . By Property (K2), h vanishes almost everywhere on A and Property (K4) implies that $h(x) = 0$ for a.e. $x \in \mathbb{R}^n \setminus B_\epsilon$. But $\epsilon > 0$ was arbitrary, which implies that $h(x) = 0$ a.e., contradicting Property (K3) and proving (2.10).

Using a change of coordinates, (2.10) implies that $d_\epsilon(x) > 0$ for any $\epsilon > 0$ and $x \in \bar{\Omega}$. Since Ω is bounded and d_ϵ is continuous, by compactness of $\bar{\Omega}$ d_ϵ takes its minimum value at some point $x_0 \in \bar{\Omega}$. The statement of the proposition follows by setting $c_\epsilon = d_\epsilon(x_0)$, giving $d_\epsilon(x) \geq c_\epsilon > 0$. \square

Let $\Omega \subseteq \mathbb{R}^n$ and $\epsilon_0 > 0$ be such that d_ϵ satisfies Proposition 2.7 for every $\epsilon \in (0, \epsilon_0)$. Then, for every such ϵ , $p_\epsilon : \Omega \times \Omega \rightarrow \mathbb{R}$ with

$$(2.11) \quad p_\epsilon(x, y) = \frac{k_\epsilon(x, y)}{d_\epsilon(x)}$$

is a well-defined measurable function on $\Omega \times \Omega$. By construction, this function satisfies $p_\epsilon(x, y) \geq 0$ and $\int_{\Omega} p_\epsilon(x, s) ds = 1$ for every $x, y \in \Omega$, and is therefore a Markov kernel. Note that, unlike k_ϵ , p_ϵ is in general neither translation-invariant nor symmetric. The procedure to obtain p_ϵ from k_ϵ is sometimes referred to as left normalization; e.g., [2].

2.5. Smoothing using Markovian kernels. Similarly to the kernel k_ϵ , the Markov kernel p_ϵ from (2.11) has an associated bounded integral operator $P_\epsilon : L^1(\Omega) \rightarrow L^1(\Omega)$, defined as

$$(2.12) \quad P_\epsilon f = \int_{\Omega} p_\epsilon(\cdot, y) f(y) dy.$$

We have $P_\epsilon 1_\Omega = 1_\Omega$ from which it follows that P_ϵ preserves constant functions on Ω . If Ω is bounded, we have $L^p(\Omega) \subseteq L^1(\Omega)$ for all $p \in [1, \infty]$, and thus P_ϵ is well-defined

as a bounded operator from $L^p(\Omega)$ into $L^1(\Omega)$. Since K_ϵ maps $L^\infty(\mathbb{R}^n)$ to $C_b(\mathbb{R}^n)$ and $1/d_\epsilon$ is bounded and continuous (the latter, by Proposition 2.7), we have that P_ϵ maps functions in $L^\infty(\Omega)$ to continuous bounded functions on Ω .

By the above facts and Lemma 2.2, we think of P_ϵ as a smoothing operator on $L^p(\Omega)$ that preserves constant functions. Given a function $f \in L^p(\Omega)$, we will employ $P_\epsilon f$ as an approximation to f . The following theorem is our main result that establishes the convergence properties of this approximation under suitable assumptions on the domain and kernel.

THEOREM 2.8. *Let Ω be a thick open subset of \mathbb{R}^n , and suppose that the shape function h satisfies Properties (K1)–(K4). Then, there exists $\epsilon_0 > 0$ such that for every $p \in [1, \infty]$, $\{P_\epsilon\}_{0 < \epsilon < \epsilon_0}$ from (2.12) is a uniformly bounded family of operators from $L^p(\Omega)$ to itself. If, in addition, h satisfies the decay bound $|h(x)| \leq C(1 + \|x\|)^{-(n+\delta)}$ for some $C, \delta > 0$, the following hold.*

1. For every $p \in (1, \infty]$ and $f \in L^p(\Omega)$, $P_\epsilon f$ converges to f a.e.
2. For every $p \in (1, \infty)$ and $f \in L^p(\Omega)$, $P_\epsilon f$ converges to f in $L^p(\Omega)$ norm.
3. If h lies in $L^1(\mathbb{R}^n) \cap L^q(\mathbb{R}^n)$ with $\frac{1}{p} + \frac{1}{q} = 1$, then for every $p \in (1, \infty]$ and $f \in L^p(\Omega)$ $P_\epsilon f$ lies in $C_b(\Omega)$.
4. If Ω is bounded and $h \in L^1(\mathbb{R}^n) \cap H^r(\mathbb{R}^n)$, then for every $f \in L^2(\Omega)$ $P_\epsilon f$ lies in $C^r(\Omega)$.

Proof. See subsection 3.3. □

3. Convergence analysis. The focus of this section will be on proving Proposition 2.7 and Theorem 2.8. We begin by deriving some auxiliary results on thick sets (subsection 3.1) used in the proof of Proposition 2.7. We then examine the case of smoothing bounded measurable functions (subsection 3.2). We prove Theorem 2.8 in subsection 3.3 using the results from subsections 3.1 and 3.2.

3.1. Convolution and thick open sets. We prove a technical lemma that addresses Claim 2 of Proposition 2.7. The goal is to leverage thickness of Ω to deduce that for a given shape function h and for small-enough $\epsilon > 0$ (as well as in the limit), the degree function $d_\epsilon = h_\epsilon * 1_\Omega$ from (2.9) satisfies $d_\epsilon(x) \geq c > 0$ for every $x \in \bar{\Omega}$. Let us first review a few examples and non-examples of thick open sets.

A non-example. We construct a (non-thick) bounded open subset $\Omega \subset \mathbb{R}$ with no strictly positive lower bound for $l_\epsilon * 1_\Omega$. To a map $r : \mathbb{N} \rightarrow [0, 1]$ we associate an open set $\Omega = \bigcup_{n=1}^\infty (a_n, b_n)$, where $\frac{1}{n+1} \leq a_n < b_n \leq \frac{1}{n}$ and

$$b_n + a_n = \frac{1}{n} + \frac{1}{n+1}, \quad b_n - a_n = r_n \left(\frac{1}{n} - \frac{1}{n+1} \right).$$

Intuitively, (a_n, b_n) is an interval centered at the center of $I = \left(\frac{1}{n+1}, \frac{1}{n} \right)$ that covers a fraction r_n of the length (Lebesgue measure) of I . For $\epsilon = \frac{1}{2n} - \frac{1}{2n+2} = \frac{1}{2n(n+1)}$ and the center point $x_n = \frac{1}{2n} + \frac{1}{2n+2}$ we have

$$l_\epsilon * 1_\Omega(x_n) = \frac{|B_\epsilon(x_n) \cap \Omega|}{|B_\epsilon(x_n)|} = r_n,$$

and we conclude that if $r_n \rightarrow 0$ then Ω is not thick, i.e., there is no lower bound for $l_\epsilon * 1_\Omega$ as $\epsilon \rightarrow 0$.

Triangles. A triangle in \mathbb{R}^2 is thick. It is not hard to see that if θ is the smallest angle in a given triangle Ω , then for small enough $\epsilon > 0$ we have $l_\epsilon * 1_\Omega(x) \geq \frac{\theta}{2\pi}$ for any $x \in \Omega$.

Finite unions of thick sets. Let Ω_n be a finite collection of thick sets such that for small $\epsilon > 0$, $l_\epsilon * 1_{\Omega_n}(x) \geq c_n$. Then, $\Omega = \bigcup_n \Omega_n$ is a thick set with $l_\epsilon * 1_\Omega(x) \geq \min c_n$. In particular, a finite union of triangles is thick, and this includes polygons and more general irregular domain regions formed by finitely many triangles.

LEMMA 3.1. *Let Ω be a thick open subset of \mathbb{R}^n and h a shape function satisfying Properties (K1)–(K3). Then, there exists $c, \epsilon_0 > 0$ such that for every $\epsilon \in (0, \epsilon_0)$ and $x \in \Omega$, we have*

$$d_\epsilon(x) \equiv h_\epsilon * 1_\Omega(x) \geq c.$$

Proof. For any $\delta > 0$, there exists a simple radial function $\tilde{h} \geq 0$ satisfying $\|h - \tilde{h}\|_{L^1(\mathbb{R}^n)} < \delta$. Such \tilde{h} can be expressed as a finite sum $\tilde{h}(x) = \sum_{i=1}^s c_i l_{r_i}(x)$, where $s \in \mathbb{N}$, $l_r(x) = r^{-n} 1_B(x/r)$, $\sum_{i=1}^s c_i = \int_{\mathbb{R}^n} \tilde{h}(x) dx = 1$, and $c_i \geq 0$. Note that $\|l_r\|_{L^1(\mathbb{R}^n)} = 1$. Since Ω is thick, there exist $c, \epsilon_0 > 0$ such that for every $i \in \{1, \dots, s\}$, $\epsilon \in (0, \epsilon_0)$, and $x \in \Omega$, we have $l_{\epsilon r_i} * 1_\Omega(x) > c$. But the same lower bound, c , applies to any convex combination of $l_{\epsilon r_i} * 1_\Omega(x)$, and thus

$$(3.1) \quad h'_\epsilon * 1_\Omega(x) = \sum_{i=1}^s c_i l_{\epsilon r_i} * 1_\Omega(x) > c.$$

On the other hand, from Lemma 2.1, we have

$$(3.2) \quad \|h_\epsilon * 1_\Omega - h'_\epsilon * 1_\Omega\|_\infty \leq \|h - h'\|_{L^1(\mathbb{R}^n)} < \delta.$$

Combining (3.1) and (3.2), we conclude that for every $x \in \Omega$, $h_\epsilon * 1_\Omega(x) > c - \delta$. Since $\delta > 0$ was arbitrary, we have $h_\epsilon * 1_\Omega(x) \geq c$. Moreover, since d_ϵ is continuous as a function on \mathbb{R}^n , the bound holds for every $x \in \bar{\Omega}$. \square

3.2. Smoothing bounded measurable functions. In this subsection, we discuss convergence of $K_\epsilon f$ where f is a bounded measurable function, and we use it to determine the limiting behavior of K_ϵ as $\epsilon \rightarrow 0$. The following proposition shows that for bounded measurable functions, the Lebesgue differentiation results discussed in subsection 2.3 apply to more general families of kernels than the tophat kernels.

PROPOSITION 3.2. *Let h be a shape function satisfying Properties (K1)–(K3) and K_ϵ be the associated integral operator from (2.3). Then, for every bounded, measurable function $f : \mathbb{R}^n \rightarrow \mathbb{R}$,*

$$\lim_{\epsilon \rightarrow 0} K_\epsilon f(x) = \tilde{f}(x) \equiv \lim_{\epsilon \rightarrow 0} \frac{1}{|B_\epsilon(x)|} \int_{B_\epsilon(x)} f(y) dy$$

for every $x \in \mathbb{R}^n$, provided that the limit on the right hand side exists.

Proof. Without loss of generality, we prove the statement for $x = 0 \in \mathbb{R}^n$ and a positive bounded function f , i.e., we prove $K_\epsilon f(0) = h_\epsilon * f(0) \rightarrow \tilde{f}(0)$. Let $h^{(j)}$ be an increasing sequence of simple functions of the form $h^{(j)}(x) = \sum_{i=1}^{s_j} C_{j,i} 1_{B_{j,i}}$, $s_j \in \mathbb{N}$, that converge to h from below such that $\|h - h^{(j)}\|_{L^1(\mathbb{R}^n)} = \delta_j$. Here, $B_{j,i} \subset \mathbb{R}^n$ is a ball centered at the origin, and

$$(3.3) \quad \sum_i^{s_j} C_{j,i} |B_{j,i}| = 1 - \delta_j$$

with $\delta_j \rightarrow 0$. Note that since $\int_{\mathbb{R}^n} h(x)f(x) dx < \infty$ and $h^{(j)} f \nearrow hf$, by the monotone convergence theorem, $\int_{\mathbb{R}^n} h(x)f(x) dx = \lim_{j \rightarrow \infty} \int_{\mathbb{R}^n} h^{(j)}(x)f(x) dx$. This allows us

to express the limit of $K_\epsilon f(0)$ as $\epsilon \rightarrow 0$ as

$$\begin{aligned} \lim_{\epsilon \rightarrow 0} K_\epsilon f(0) &= \lim_{\epsilon \rightarrow 0} \int_{\mathbb{R}^n} h_\epsilon(x) f(x) dx = \lim_{\epsilon \rightarrow 0} \int_{\mathbb{R}^n} \epsilon^{-n} h(x/\epsilon) f(x) dx \\ &= \lim_{\epsilon \rightarrow 0} \lim_{n \rightarrow \infty} \int_{\mathbb{R}^n} h^{(j)}(y) f(y\epsilon) dy, \end{aligned}$$

where we made the change of variables $y = x/\epsilon$. Next, let $\epsilon = 1/m$, $a_{j,m} = \int_{\mathbb{R}^n} h^{(j)}(y) f(y/m) dy$, and $a_m = \int_{\mathbb{R}^n} h(y) f(y/m) dy$. To apply the Moore-Osgood theorem and interchange the order of limits in j and m , we show the uniform convergence $a_{j,m} \rightarrow a_m$ as $j \rightarrow \infty$ with respect to $m \in \mathbb{N}$. Let M be an upper bound for $|f|$. For any $\tilde{\epsilon} > 0$ and $m \in \mathbb{N}$, there exists $j_* \in \mathbb{N}$ such that for all $j \geq j_*$, $\|h^{(j)} - h\|_{L^1(\mathbb{R}^n)} \leq \tilde{\epsilon}/M$. This implies,

$$|a_{j,m} - a_m| = \left| \int_{\mathbb{R}^n} \left(h^{(j)}(y) - h(y) \right) f(y/m) dy \right| \leq M \int_{\mathbb{R}^n} \left| h^{(j)}(y) - h(y) \right| dy \leq \tilde{\epsilon},$$

and we conclude that the convergence of $a_{j,m}$ to a_m is uniform with respect to $m \in \mathbb{N}$. After switching the order of limits in (3.4), we get

$$\begin{aligned} \lim_{\epsilon \rightarrow 0} K_\epsilon f(0) &= \lim_{j \rightarrow \infty} \lim_{\epsilon \rightarrow 0} \int_{\mathbb{R}^n} h^{(j)}(y) f(y\epsilon) dy = \lim_{j \rightarrow \infty} \lim_{\epsilon \rightarrow 0} \int_{\mathbb{R}^n} \epsilon^{-n} h^{(j)}(x/\epsilon) f(x) dx \\ &= \lim_{j \rightarrow \infty} \lim_{\epsilon \rightarrow 0} \int_{\mathbb{R}^n} \epsilon^{-n} \sum_{i=1}^{s_j} C_{j,i} \mathbf{1}_{\epsilon B_{j,i}}(x) f(x) dx \\ &= \lim_{j \rightarrow \infty} \lim_{\epsilon \rightarrow 0} \sum_{i=1}^{s_j} \epsilon^{-n} C_{j,i} \int_{\epsilon B_{j,i}} f(x) dx \\ &= \lim_{j \rightarrow \infty} \sum_{i=1}^{s_j} C_{j,i} |B_{j,i}| \lim_{\epsilon \rightarrow 0} \frac{1}{|\epsilon B_{j,i}|} \int_{\epsilon B_{j,i}} f(x) dx \\ &= \lim_{j \rightarrow \infty} \sum_{i=1}^{s_j} C_{j,i} |B_{j,i}| \tilde{f}(0) = \tilde{f}(0), \end{aligned}$$

where we used (3.3) to arrive at the last equality. \square

COROLLARY 3.3. *Under the assumptions of Proposition 3.2, the degree functions d_ϵ from (2.9) associated with h and a measurable set $\Omega \subseteq \mathbb{R}^n$ satisfy $\lim_{\epsilon \rightarrow 0} d_\epsilon(x) = \rho_\Omega(x)$ for $x \in \Omega$, where ρ_Ω is the Lebesgue density function of Ω from (2.8).*

Proof. The claim follows by taking $f = \mathbf{1}_\Omega$ and applying Proposition 3.2. \square

Proposition 3.2 and Corollary 3.3 lead to a pointwise convergence result for $P_\epsilon f$. In subsection 3.3, we will prove a stronger version of the following corollary:

COROLLARY 3.4. *Let Ω be a thick open set in \mathbb{R}^n . Let $h \in L^1(\mathbb{R}^n)$ be a function satisfying Properties (K1)–(K3) and P_ϵ the associated Markovian integral operator from (2.12). Then, for every bounded measurable function $f : \Omega \rightarrow \mathbb{R}$ and point x in the interior of Ω we have, $\lim_{\epsilon \rightarrow 0} P_\epsilon f(x) = \tilde{f}(x)$, with \tilde{f} defined as in Proposition 3.2. In particular, $\lim_{\epsilon \rightarrow 0} P_\epsilon f(x) = f(x)$ a.e. on $\tilde{\Omega}$.*

Proof. Recall that $P_\epsilon f(x) = K_\epsilon f(x)/d_\epsilon(x)$, where $d_\epsilon(x)$ is bounded away from zero by Lemma 3.1. Moreover, by Corollary 3.3 we have $\lim_{\epsilon \rightarrow 0} d_\epsilon(x) = \rho_\Omega(x) = 1$ for every x in the interior of Ω . The claim then follows by extending f by zero to a function on \mathbb{R}^n and applying Proposition 3.2 to obtain $\lim_{\epsilon \rightarrow 0} K_\epsilon f(x) = \tilde{f}(x)/\rho_\Omega(x) = \tilde{f}(x)$. \square

3.3. Proof of Theorem 2.8. We seek analogs of Theorems 2.3 and 2.4 for the case where convolution by the function h_ϵ (equivalently, integration against the translation-invariant kernel k_ϵ) is replaced by integration against the Markov-normalized kernel p_ϵ from (2.11) over the thick open set $\Omega \subseteq \mathbb{R}^n$. Note that for a generic Ω , the kernel p_ϵ is no longer translation-invariant and it has non-trivial behavior near the boundary of Ω . In particular, $P_\epsilon f(x)$ can blow up if $d_\epsilon(x) \rightarrow 0$ at $x \in \partial\Omega$.

Let Ω be a thick open set and $h \in L^1(\mathbb{R}^n)$ a shape function. For $\epsilon_0 > 0$ chosen according to Definition 2.6, $p_\epsilon : \Omega \times \Omega \rightarrow \mathbb{R}$ defined in (2.11), and $f \in L^p(\Omega)$, we define the Markovian local maximal function on Ω by

$$M_h^\Omega f(x) = \sup_{0 < \epsilon < \epsilon_0} \left| \int_\Omega p_\epsilon(x, y) f(y) dy \right|.$$

Note that, unlike the classical definition in (2.6), the range for the parameter ϵ is restricted to the interval $(0, \epsilon_0)$ where we have a strictly positive lower bound for $l_\epsilon * 1_\Omega$. We then have:

PROPOSITION 3.5. *Let $\Omega \subseteq \mathbb{R}^n$ be a thick open set and $h \in L^1(\mathbb{R}^n)$ a shape function satisfying Properties (K1)–(K4). Then, for every $p \in (1, \infty]$ there exists $\tilde{A} > 0$ such that for every $f \in L^p(\Omega)$ we have*

$$\|M_h^\Omega f\|_{L^p(\Omega)} \leq \tilde{A} \|f\|_{L^p(\Omega)}.$$

Proof. By Lemma 3.1, thickness of Ω implies that there exists $c > 0$ such that $h_\epsilon * 1_\Omega(x) \geq c > 0$ for every $\epsilon \in (0, \epsilon_0)$ and $x \in \Omega$. Using the definition of the maximal function $M_h f$ in (2.6), we get

$$\left| \int_\Omega p_\epsilon(x, y) f(y) dy \right| = \frac{|h_\epsilon * f(x)|}{h_\epsilon * 1_\Omega(x)} \leq c^{-1} |h_\epsilon * f(x)| \leq c^{-1} M_h f(x),$$

for every $x \in \Omega$. Meanwhile, using Theorem 2.3, we have $\|M_h f\|_{L^p(\Omega)} \leq A \|f\|_{L^p(\Omega)}$, where we have identified f with a function on \mathbb{R}^n that vanishes on $\mathbb{R}^n \setminus \Omega$. Combining the last two bounds, we obtain

$$\|M_h^\Omega f\|_{L^p(\Omega)} \leq c^{-1} \|M_h f\|_{L^p(\Omega)} \leq c^{-1} A \|f\|_{L^p(\Omega)},$$

and the claim of the proposition follows with $\tilde{A} = c^{-1} A$. \square

COROLLARY 3.6. *The integral operators $\{P_\epsilon\}_{0 < \epsilon < \epsilon_0}$ from (2.12) are well-defined and uniformly bounded on $L^p(\Omega)$ for every $p \in [1, \infty]$.*

Proof. The well-definition and uniform boundedness of $P_\epsilon : L^1(\Omega) \rightarrow L^1(\Omega)$ for $0 < \epsilon < \epsilon_0$ follows by construction of the kernel p_ϵ in (2.11) under Properties (K1)–(K4) and thickness of Ω ; see subsections 2.3 and 2.4. In the case $p \in (1, \infty]$, for any $\epsilon \in (0, \epsilon_0)$ and $f \in L^p(\Omega)$ we have $\|P_\epsilon f\|_{L^p(\Omega)} \leq \|M_h^\Omega f\|_{L^p(\Omega)}$. The claim follows from Proposition 3.5 with $P_\epsilon : L^p(\Omega) \rightarrow L^p(\Omega)$ bounded in operator norm by \tilde{A} . \square

PROPOSITION 3.7. *Let $\Omega \subseteq \mathbb{R}^n$ be a thick open set and h a shape function satisfying Properties (K1)–(K4) and the decay bound $|h(x)| \leq C(1 + \|x\|)^{-(n+\delta)}$ for some $C, \delta > 0$. Let P_ϵ be the induced Markovian integral operators from (2.12). Then, for every $f \in L^p(\Omega)$ with $1 < p \leq \infty$, $P_\epsilon f$ converges to f a.e. as $\epsilon \rightarrow 0^+$.*

Proof. By Corollary 3.3, we have $\lim_{\epsilon \rightarrow 0^+} h_\epsilon * 1_\Omega(x) = 1$ for every interior point $x \in \Omega$. and by Theorem 2.4 $\lim_{\epsilon \rightarrow 0^+} h_\epsilon * f = f(x)$ for a.e. $x \in \Omega$. Thus, for a.e. $x \in \Omega$, we have

$$\lim_{\epsilon \rightarrow 0^+} P_\epsilon f(x) = \frac{\lim_{\epsilon \rightarrow 0^+} h_\epsilon * f(x)}{\lim_{\epsilon \rightarrow 0^+} h_\epsilon * 1_\Omega(x)} = f(x). \quad \square$$

Remark 3.8. The thickness of Ω is an important constraint for $h_\epsilon * f$ to lie in $L^p(\Omega)$ and here is another way of looking at this condition. By Lemma 3.1, thickness of Ω is equivalent to the uniform boundedness of

$$\frac{1}{l_\epsilon * 1_\Omega(x)} = \frac{|B_\epsilon(x)|}{|B_\epsilon(x) \cap \Omega|} \in L^\infty(\Omega),$$

and we can then conclude that

$$\left\| \frac{1}{d_\epsilon} \cdot h_\epsilon * f \right\|_{L^p(\Omega)} \leq c^{-1} \|h_\epsilon * f\|_{L^p(\Omega)} \leq c^{-1} A \|f\|_{L^p(\Omega)}.$$

However, multiplication by $\frac{1}{d_\epsilon}$ is a bounded operator on $L^p(\Omega)$ if and only if $\frac{1}{d_\epsilon}$ lies in $L^\infty(\Omega)$. This suggests that if Ω is not thick then P_ϵ may not even be a bounded operator on $L^p(\Omega)$.

We are now ready to prove Theorem 2.8.

Proof of Theorem 2.8. The well-definition and boundedness of $P_\epsilon : L^p(\Omega) \rightarrow L^p(\Omega)$ for $p \in [1, \infty]$ is proved by Corollary 3.6. Claim 1 is proved by Proposition 3.7.

Turning to Claim 2, by the dominated convergence theorem for $L^p(\Omega)$, if the sequence $f_j := P_{1/j} f \in L^p(\Omega)$ converges as $j \rightarrow \infty$ a.e. to f and the terms f_j are dominated in by some function in $L^p(\Omega)$, then f_j converges to f in $L^p(\Omega)$ norm. Thus, since we have a.e. convergence of $P_\epsilon f$ to f from Claim 1, to prove Claim 2 it suffices to show that $f_j \leq F$ for some $F \in L^p(\Omega)$. Indeed, by Proposition 3.5, we have that for every $\epsilon \in (0, \epsilon_0)$ g_ϵ is bounded in $L^p(\Omega)$ by $M_h^\Omega f$. Setting $F = M_h^\Omega$ thus proves Claim 2.

Next, to prove Claim 3 we use Lemma 2.1 to deduce that $K_\epsilon f$ lies $C_b(\Omega)$ for every $f \in L^p(\Omega)$ with $\frac{1}{p} + \frac{1}{q} = 1$. That $P_\epsilon f = \frac{K_\epsilon f}{d_\epsilon}$ also lies in $C_b(\Omega)$ then follows from the fact that $\frac{1}{d_\epsilon} \in C_b(\Omega)$ by Lemma 3.1. Finally, to prove Claim 4, if $h \in L^1(\mathbb{R}^n) \cap H^r(\mathbb{R}^n)$ it follows from Lemma 2.2 that for every $f \in L^2(\Omega)$ $K_\epsilon f$ lies in $C^r(\Omega)$. If Ω is bounded, we have $d_\epsilon \in C^r(\Omega)$ since $1_\Omega \in L^2(\Omega)$, and since, by Lemma 3.1, $d_\epsilon(x) \geq c > 0$ on Ω we also have $\frac{1}{d_\epsilon} \in C^r(\Omega)$. Thus, $P_\epsilon f = \frac{K_\epsilon f}{d_\epsilon}$ lies in $C^r(\Omega)$. \square

4. Thick sets as metric measure spaces. Recall that a metric measure space (X, d, μ) is doubling [21] if there exists $M > 0$ such that for any $r > 0$ and $x \in X$,

$$(4.1) \quad \mu(B_{2r}(x)) \leq M\mu(B_r(x)).$$

The base-2 logarithm of the optimal such constant M is known as the doubling dimension of (X, d, μ) . We will say that (M, d, μ) is locally doubling if (4.1) holds for all $r \in (0, r_0)$ for some $r_0 > 0$. Given a measurable set $\Omega \subseteq \mathbb{R}^n$, we consider the measure space (Ω, d, μ) , where d and μ are the Lebesgue measure Euclidean distance induced from \mathbb{R}^n , respectively.

PROPOSITION 4.1. *If $\Omega \subseteq \mathbb{R}^n$ is a thick measurable set then (Ω, d, μ) is locally doubling.*

Proof. Since Ω is thick, there exist $r_0 > 0$ and $c > 0$ such that for all $r \in (0, r_0)$ $|B_r(x) \cap \Omega| \geq c|B_r(x)|$. Therefore,

$$\mu(B_{2r}(x)) = |B_{2r}(x) \cap \Omega| \leq |B_{2r}(x)| \leq M|B_r(x)| \leq \frac{M}{c}|B_r(x) \cap \Omega| = \frac{M}{c}\mu(B_r(x)),$$

showing that Ω satisfies the doubling inequality for $r < r_0$. \square

The following proposition establishes that thickness and the doubling property are independent notions.

PROPOSITION 4.2.

1. *There exist thick measurable sets $\Omega \subset \mathbb{R}^n$ such that (Ω, d, μ) is not doubling.*
2. *There exist doubling metric measure spaces (Ω, d, μ) , $\Omega \subset \mathbb{R}^n$, such that Ω is not thick.*

Proof. Starting from Claim 1, we build explicit examples of thick measurable sets that are not doubling by considering the following family of subsets of \mathbb{R}^n . Let $x \in \mathbb{R}^n$ and for $0 \leq \alpha, \beta < \frac{1}{2}$ define

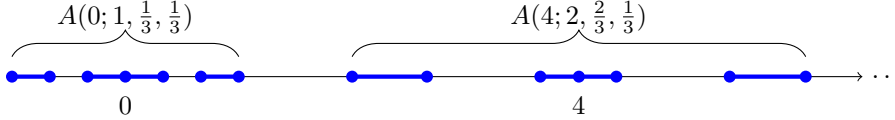
$$A(x; r, \alpha, \beta) = B_r(x) \setminus (B_{r-\alpha r}(x) \setminus B_{\beta r}(x)).$$

In two dimensions, these sets can be constructed by removing an annulus from a disc of radius r centered at x . For simplicity, for the rest of this proof we set $n = 1$.

Choosing a countable collection of $x_j, r_j \in \mathbb{R}$ such that the corresponding balls, $B_{r_j}(x_j)$, are disjoint, we define $\Omega \subset \mathbb{R}$ as the disjoint union $\Omega = \bigcup_{j=1}^{\infty} A(x_j; r_j, \alpha_j, \beta_j)$, with $0 \leq \alpha_j, \beta_j < \frac{1}{2}$ and $r_j > 0$. Making the observation

$$\frac{\mu(B_{r_j}(x_j))}{\mu(B_{r_j/2}(x_j))} = \frac{r_j - (r_j - \alpha_j r_j) + \beta_j r_j}{\beta_j r_j} = 1 + \frac{\alpha_j}{\beta_j},$$

it is not hard to see that (Ω, d, μ) is doubling only if α_j/β_j is a bounded sequence. On the other hand, setting $\alpha_j = 1/3$, $\beta_j = 1/(3j)$, and $r_j = j$, then Ω is thick (since each connected component of Ω has length at least $1/3$) but does not satisfy the doubling property at the center points x_j as $j \rightarrow \infty$ (see the figure below).



To prove Claim 2, let $\Omega = \{x = (x_1, x_2) \in \mathbb{R}^2 : 0 \leq x_1, 0 \leq x_2 \leq \frac{1}{x_1}\}$. This set is not thick, however, (Ω, d, μ) is doubling with doubling dimension 2. \square

5. Bistochastic kernels. In this subsection we consider an alternative kernel normalization procedure than the approach described in subsection 2.4, leading to a bistochastic kernel whose corresponding integral operators preserve constant functions as well as integrals of functions. Our approach is based on the class of bistochastic kernels studied by Coifman and Hirn in [9] which was adapted in [13] to a setting closer to the function smoothing problem studied in this paper.

Assuming, as in subsection 2.4, that $\Omega \subseteq \mathbb{R}^n$ is a thick open set so Proposition 2.7 holds for every $\epsilon \in (0, \epsilon_0)$, $\epsilon_0 > 0$, we define the normalization function $q_\epsilon : \mathbb{R}^n \rightarrow \mathbb{R}_+$ as

$$(5.1) \quad q_\epsilon = K_\epsilon \left(\frac{1_\Omega}{d_\epsilon} \right) \equiv \int_\Omega \frac{k_\epsilon(x, y)}{d_\epsilon(y)} dy.$$

Since $\frac{1_\Omega}{d_\epsilon} \in L^\infty(\mathbb{R}^n)$, it follows from Lemma 2.1 that $q_\epsilon \in C_b(\mathbb{R}^n)$. In particular, since $c \leq d_\epsilon \leq 1$ on Ω (see Lemma 3.1), we have

$$c \leq K_\epsilon 1_\Omega(x) \leq K_\epsilon \left(\frac{1_\Omega}{d_\epsilon(x)} \right) \leq \frac{1}{c} K_\epsilon 1_\Omega(x) \leq \frac{1}{c},$$

and we deduce that q_ϵ is bounded above and bounded away from 0 from below, $c \leq q_\epsilon \leq c^{-1}$. As a result, $\tilde{p}_\epsilon : \Omega \times \Omega \rightarrow \mathbb{R}$ with

$$(5.2) \quad \tilde{p}_\epsilon(x, y) = \int_{\Omega} \frac{k_\epsilon(x, z)k_\epsilon(z, y)}{d_\epsilon(x)q_\epsilon(z)d_\epsilon(y)} dz$$

is a well-defined, measurable kernel. Note the use of right normalization of k_ϵ in the definition (5.1) of q_ϵ as opposed to left normalization employed in (2.11) to build the kernel p_ϵ .

One readily verifies that

$$\tilde{p}_\epsilon(x, y) = \tilde{p}_\epsilon(y, x), \quad \tilde{p}_\epsilon(x, y) \geq 0, \quad \int_{\mathbb{R}^n} \tilde{p}_\epsilon(x, z) dz = 1,$$

for every $x, y \in \Omega$; that is, \tilde{p}_ϵ is a symmetric (bistochastic) Markov kernel on Ω . Moreover, defining $\tilde{P}_\epsilon : L^1(\mathbb{R}^n) \rightarrow L^1(\mathbb{R}^n)$ as

$$(5.3) \quad \tilde{P}_\epsilon f(x) = \int_{\Omega} \tilde{p}_\epsilon(x, y) f(y) dy,$$

it follows from symmetry of \tilde{p}_ϵ that \tilde{P}_ϵ preserves integrals of functions,

$$(5.4) \quad \int_{\Omega} \tilde{P}_\epsilon f(x) dx = \int_{\Omega} f(x) dx, \quad \forall f \in L^1(\Omega).$$

In addition, we have $\|\tilde{P}_\epsilon f\|_{L^1(\Omega)} \leq \|f\|_{L^1(\Omega)}$ so \tilde{P}_ϵ is a contraction on $L^1(\Omega)$. If $f \in L^1(\mu)$ is the density of a measure ν_f on Ω with respect to Lebesgue measure, (5.4) implies that $\nu_f(\Omega) = \nu_{\tilde{P}_\epsilon f}(\Omega)$ so we can think of \tilde{P}_ϵ as a mass-preserving operator.

The following is an analogous convergence result to Theorem 2.8 for integral operators induced by the bistochastic kernels from (5.2).

THEOREM 5.1. *Let Ω be a thick open subset of \mathbb{R}^n , and suppose that the shape function h satisfies Properties (K1)–(K4). Then, there exists $\epsilon_0 > 0$ such that for every $p \in [1, \infty]$, $\{\tilde{P}_\epsilon\}_{0 < \epsilon < \epsilon_0}$ from (5.3) is a uniformly bounded family of operators from $L^p(\Omega)$ to itself. In addition, if Ω is bounded and h satisfies the decay bound $|h(x)| \leq C(1 + \|x\|)^{-(n+\delta)}$ for some $C, \delta > 0$, the following hold.*

1. *For every $p \in (1, \infty)$ and $f \in L^p(\Omega)$, $\tilde{P}_\epsilon f$ converges to f in $L^p(\Omega)$ norm.*
2. *If h lies in $L^1(\mathbb{R}^n) \cap L^q(\mathbb{R}^n)$ with $\frac{1}{p} + \frac{1}{q} = 1$, then for every $p \in (1, \infty]$ and $f \in L^p(\Omega)$, $\tilde{P}_\epsilon f$ lies in $C_b(\Omega)$.*
3. *If $h \in L^1(\mathbb{R}^n) \cap H^r(\mathbb{R}^n)$, then for every $f \in L^2(\Omega)$ $\tilde{P}_\epsilon f$ lies in $C^r(\Omega)$.*

Note that Theorem 5.1 is somewhat weaker than Theorem 2.8 in that it requires that Ω is bounded and does not make a claim about pointwise convergence of $\tilde{P}_\epsilon f$ to f . For the proof of Theorem 5.1 we will make use of the following result.

LEMMA 5.2. *Let $\Omega \subseteq \mathbb{R}^n$ be a measurable set, and consider $f \in L^\infty(\Omega)$ and $\{f_\epsilon \in L^\infty(\Omega)\}_{0 < \epsilon < \epsilon_0}$ where the f_ϵ are uniformly bounded in $L^\infty(\Omega)$. For $p \in [1, \infty)$, let $M_f : L^p(\Omega) \rightarrow L^p(\Omega)$ (resp. $M_{f_\epsilon} : L^p(\Omega) \rightarrow L^p(\Omega)$) be the multiplication operator by f (resp. f_ϵ). Then, if f_ϵ converges in $L^p(\Omega)$ to f as $\epsilon \rightarrow 0$, M_{f_ϵ} converges to M_f in the strong operator topology of $B(L^p(\Omega))$.*

Proof. See Appendix A. □

Proof of Theorem 5.1. Observe that

$$(5.5) \quad \tilde{P}_\epsilon = P_\epsilon \circ M_{1/q_\epsilon} \circ P_\epsilon \circ M_{1/d_\epsilon},$$



FIG. 1. Piecewise-continuous mass density function $m(x)$ associated with two ice floes (left) and the corresponding smooth mass density field obtained by smoothing m by a Markovian integral operator (right).

where M_{1/d_ϵ} and M_{1/q_ϵ} are the multiplication operators by $1/d_\epsilon$ and $1/q_\epsilon$, respectively. Since $d_\epsilon \leq c$ and $q_\epsilon \geq c$, we have that for every $p \in [1, \infty]$, $\{M_{1/d_\epsilon}\}_{0 < \epsilon < \epsilon_0}$ and $\{M_{1/q_\epsilon}\}_{0 < \epsilon < \epsilon_0}$ are uniformly bounded families of operators on $L^p(\Omega)$. Since, by Theorem 2.8, $\{P_\epsilon\}_{0 < \epsilon < \epsilon_0}$ is also uniformly bounded, it follows that $\{\tilde{P}_\epsilon\}_{0 < \epsilon < \epsilon_0}$ is uniformly bounded on $L^p(\Omega)$, as claimed.

Consider now Claim 1. Since Ω is bounded and $c \leq d_\epsilon \leq 1$, d_ϵ and $1/d_\epsilon$ lie in $L^p(\Omega)$ for all $p \in [1, \infty]$. By Corollary 2.5, for every $p \in (1, \infty)$, $d_\epsilon = K_\epsilon 1_\Omega$ converges to 1_Ω in $L^p(\Omega)$. Moreover, we have

$$\left\| 1_\Omega - \frac{1}{d_\epsilon} \right\|_{L^p(\Omega)} = \left\| \frac{d_\epsilon - 1_\Omega}{d_\epsilon} \right\|_{L^p(\Omega)} = \left\| \frac{K_\epsilon 1_\Omega - 1_\Omega}{d_\epsilon} \right\|_{L^p(\Omega)} \leq c^{-1} \|K_\epsilon 1_\Omega - 1_\Omega\|_{L^p(\Omega)},$$

and it follows that $1/d_\epsilon$ also converges to 1_Ω in $L^p(\Omega)$. By Lemma 5.2, we deduce that, as $\epsilon \rightarrow 0$, M_{1/d_ϵ} converges strongly to the identity on $L^p(\Omega)$. One can similarly deduce from the facts that $c \leq q_\epsilon \leq c^{-1}$ and $q_\epsilon = K_\epsilon(\frac{1}{d_\epsilon})$ that M_{1/q_ϵ} converges strongly to the identity on $L^p(\Omega)$. Since the operators P_ϵ , M_{1/q_ϵ} , and M_{1/d_ϵ} are uniformly bounded in $B(L^p(\Omega))$ for $\epsilon \in (0, \epsilon_0)$, it follows from (5.5) that \tilde{P}_ϵ converges strongly to the identity; i.e., $\tilde{P}_\epsilon f$ converges to f in $L^p(\Omega)$, as claimed.

Turning to Claim 2, since M_{1/q_ϵ} , P_ϵ , and M_{1/d_ϵ} are all bounded operators, we have that for every $f \in L^p(\Omega)$, $g_\epsilon = M_{1/q_\epsilon} P_\epsilon M_{1/d_\epsilon} f$ lies in $L^p(\Omega)$, and thus $\tilde{P}_\epsilon f = P_\epsilon g_\epsilon$ lies in $C_b(\Omega)$ by Theorem 2.8. This proves the claim.

Finally, Claim 3 follows again from Theorem 2.8 in conjunction with the fact that g_ϵ from above lies in $L^2(\Omega)$ for every $f \in L^2(\Omega)$. \square

6. Numerical approximation. In this section, we consider the problem of numerically approximating the action of the integral operators introduced in sections 2 and 5 on a class of piecewise-continuous functions on a thick, bounded, open domain $\Omega \subset \mathbb{R}^2$. Specifically, we consider a finite collection of polygons $S_\ell \subseteq \Omega$ indexed by $\ell \in \Lambda$ and functions $f : \Omega \rightarrow \mathbb{R}$ of the form

$$(6.1) \quad f(x) = \sum_{\ell \in \Lambda} f_\ell(x),$$

where $f_\ell : \Omega \rightarrow \mathbb{R}$ are functions with $\text{supp } f_\ell \subseteq S_\ell$ and $f_\ell|_{S_\ell}$ bounded continuous. This class of functions is appropriate for the numerical experiments presented in section 7 where the polygons S_ℓ correspond to ice floes as represented within two-dimensional sea ice DEMs and the functions f_ℓ represent physical floe variables such as mass density; see Figure 1 for a schematic.

Our goal is to approximate functions in this class by kernel smoothed-functions $\hat{g}_\epsilon : \Omega \rightarrow \mathbb{R}$ where \hat{g}_ϵ is a continuous function that numerically approximates $P_\epsilon f$ obtained

from the Markov integral operator in (2.12) (or its bistochastic variant, \tilde{P}_ϵ from (5.3)). As a concrete example, for an input function f from (6.1) the corresponding kernel-smoothed functions $g_\epsilon := P_\epsilon f$ take the form

$$(6.2) \quad g_\epsilon(x) = \frac{1}{d_\epsilon(x)} \sum_{\ell \in \Lambda} \int_{S_\ell} k_\epsilon(x, y) f_\ell(y) dy, \quad d_\epsilon(x) = \int_{\Omega} k_\epsilon(x, y) dy.$$

By Theorem 2.8, we have $g_\epsilon \in C_b(\Omega)$ since f lies in $L^\infty(\Omega)$ by boundedness of Ω and piecewise-continuity of f .

Let $\eta_{\epsilon, x} : \Omega \rightarrow \mathbb{R}$ denote the section of the kernel k_ϵ at $x \in \Omega$, defined as $\eta_{\epsilon, x}(y) = k_\epsilon(x, y)$. From (6.2), we see that in order to approximate $g_\epsilon(x)$ at some $x \in \Omega$ it is sufficient to approximate integrals of (i) kernel-weighted functions $y \mapsto \eta_{\epsilon, x}(y) f_\ell(y)$ over the subdomains S_ℓ ; and (ii) the kernel section $y \mapsto \eta_{\epsilon, x}(y)$ over the domain Ω . In subsections 6.1–6.3, we describe methods for approximating these integrals using numerical quadrature. These methods can be modified to deal with higher-dimensional domains and/or other integral operators than P_ϵ (in particular, the bistochastic operators \tilde{P}_ϵ).

6.1. Quadrature scheme. We supplement Properties (K1)–(K4) required of the shape function h with two further assumptions:

(K5) h is continuous.

(K6) h is strictly positive.

With these assumptions, given an integration domain $Y \subseteq \Omega$ (which could be one of the subdomains S_ℓ , or the entire set Ω) and an integrand $\varphi_x : Y \rightarrow \mathbb{R}$ parameterized by $x \in \Omega$ (which could be one of the kernel-weighted functions $\eta_{\epsilon, x} f_\ell$ or the kernel section $\eta_{\epsilon, x}$), we approximate the integral $I[\varphi_x] := \int_Y \varphi_x(y) dy$ by

$$(6.3) \quad I_N[\varphi_x] := \sum_{j=1}^N w_{j,N} \varphi_x(y_{j,N}).$$

Here, $y_{1,N}, \dots, y_{N,N}$ are quadrature nodes in Y and $w_{1,N}, \dots, w_{N,N} \in \mathbb{R}_+$ are corresponding weights. Applying (6.3) to each integral in (6.2) leads to the approximation

$$(6.4) \quad \hat{g}_\epsilon(x) \equiv g_{\epsilon, \mathbf{N}}(x) := \frac{1}{d_{\epsilon, N_\Omega}(x)} \sum_{\ell \in \Lambda_t} \tilde{g}_{\epsilon, \ell, N_\ell}(x),$$

where $\mathbf{N} = (N_\Omega, N_{\ell \in \Lambda})$ is a multi-index parameterizing numerical quadrature over the domains Ω and $\{S_\ell\}_{\ell \in \Lambda_t}$, respectively, and $d_{\epsilon, N_\Omega} : \Omega \rightarrow \mathbb{R}$ and $\tilde{g}_{\epsilon, \ell, N_\ell} : \Omega \rightarrow \mathbb{R}$ are given by

$$d_{\epsilon, N_\Omega}(x) = I_{N_\Omega}[\eta_{\epsilon, x}], \quad \tilde{g}_{\epsilon, \ell, N_\ell}(x) = I_{N_\ell}[\eta_{\epsilon, x} f_{\ell, \ell}].$$

Note that by Properties (K5) and (K6), d_{ϵ, N_Ω} , $\tilde{g}_{\epsilon, \ell, N_\ell}$, and thus $g_{\epsilon, \mathbf{N}}$, are well-defined, bounded continuous functions on Ω . If, in addition, the shape function h lies in $H^r(\Omega)$, then by Theorem 2.8 $g_{\epsilon, \mathbf{N}}$ lies in $C^r(\Omega)$. We seek to choose the quadrature nodes and weights used in (6.4) such that $g_{\epsilon, \mathbf{N}}$ converges to g_ϵ in a limit of $\mathbf{N} \rightarrow \infty$, uniformly with respect to $x \in \Omega$.

There are several possible quadrature schemes that meet these objectives, of which we describe two examples: Monte Carlo methods and triangulation methods for polygonal domains.

6.2. Monte Carlo methods. In the Monte Carlo approach, we place each target integration domain Y in a bounding rectangle $R = L_1 \times L_2 \supseteq Y$ (where L_1 and L_2 are intervals), draw M independent random samples $\tilde{y}_1, \dots, \tilde{y}_M \in R$ from the Lebesgue measure on R , and set the quadrature nodes $y_{1,N}, \dots, y_{N,N}$ to any subset of $\{\tilde{y}_1, \dots, \tilde{y}_M\}$ that lies in Y (we assume that M is sufficiently large for the chosen N). The corresponding weights are chosen uniformly as $w_{j,N} = |R|/M$ where $|R|$ is the area of R . An application of the central limit theorem then leads to the classical Monte Carlo error estimate

$$(6.5) \quad |I_N[\varphi_x] - I[\varphi_x]| \simeq \frac{s_x |R|}{|Y|} N^{-1/2}, \quad s_x^2 = \int_R (\varphi_x(y) - (I[\varphi_x]))^2 dy,$$

which holds for large N with high probability; e.g., [4].

The constant s_x in (6.5) is proportional to the standard deviation of the integrand φ_x on the domain Y . For the class of bounded, continuous functions appearing in (6.2) and (6.4) as integrands, s_x is bounded over $x \in \Omega$, and we can conclude that $g_{\epsilon, N}$ with $\mathbf{N} = (N, \dots, N)$ converges uniformly to g_ϵ as $N \rightarrow \infty$.

Two important advantages of the Monte Carlo approach are its simplicity and flexibility—other than boundedness of the standard deviations s_x we had to make essentially no explicit assumptions on the properties of φ_x and/or integration domains Y . At the same time, the standard Monte Carlo scheme does not take into account any additional regularity properties that the integrands may possess that could lead to faster rates of convergence than $N^{-1/2}$. The scheme can also be inefficient in situations where Y is not well-bounded by a rectangle (meaning, $|R|/|Y|$ is large), causing many trial quadrature nodes \tilde{y}_j drawn from the Lebesgue measure on R to be discarded.

6.3. Triangulation method. To overcome the aforementioned shortcomings of the Monte Carlo approach, we use a deterministic quadrature scheme that is based on a triangulation of $\bar{\Omega}$ and the subdomains S_ℓ . This approach sacrifices some generality, as it assumes that the integration domains are polygonal and the integrands φ_x are smooth, in exchange of potentially obtaining faster convergence rates than (6.5).

We use a triangulation algorithm developed by Shewchuk [43], which is a modification of Ruppert’s algorithm for two-dimensional quality mesh generation [41]. Through this approach, we generate triangulations of $\bar{\Omega}$ and S_ℓ that satisfy constraints on the minimum angle and maximum triangle area; see Figure 2 for a schematic of this method. We use an implementation of Shewchuk’s algorithm provided in the Python library `triangle`. Additional details on numerical implementation are included in the online repository accompanying the paper.

Next, we examine the numerical quadrature error over a triangulated domain for piecewise-constant functions $f_\ell : S_\ell \rightarrow \mathbb{R}$ and the radially symmetric function $h_\epsilon : \mathbb{R}^2 \rightarrow \mathbb{R}$ induced from the Gaussian RBF in (2.1). That is, on each polygonal domain Y (where Y is either Ω or one of the subdomains S_ℓ) we are interested in approximating integrals of the form $I[\varphi_x] = \int_Y \varphi_x(y) dy$ where $\varphi_x = \eta_{\epsilon, x}$ is the kernel section induced from

$$h_\epsilon(y) = h_\epsilon(r) = \frac{1}{\epsilon\sqrt{2\pi}} e^{-\frac{r^2}{2\epsilon^2}}, \quad r = \|y\|,$$

and x is a point in Ω .

Let $\mathcal{T} = \{T_j\}_{j=1}^N$ be a triangulation of Y . For every triangle $T_j \in \mathcal{T}$ and $a, b \in T_j$ we have $|\varphi_x(a) - \varphi_x(b)| \leq \|h'_\epsilon\|_\infty \text{diam } T_j$, where $h'_\epsilon : (0, \infty) \rightarrow \mathbb{R}$ is the radial derivative of h_ϵ .

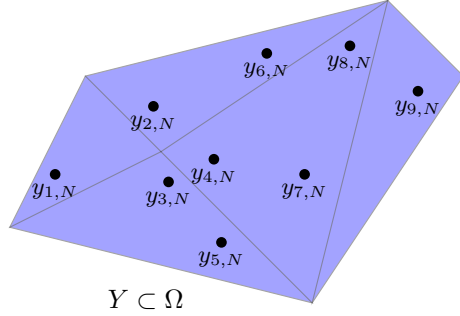


FIG. 2. Schematic of a triangulation of a single polygonal domain Y together with associated quadrature nodes $y_{j,N} \in Y$ (each coming with a corresponding weight $w_{j,N}$).

Let us obtain an upper bound for $\|h'_\epsilon\|_\infty$. We have,

$$h'_\epsilon(r) = -\frac{r}{\epsilon^2} h_\epsilon(r), \quad h''_\epsilon(r) = \left(\frac{r^2}{\epsilon^2} - 1\right) \frac{h_\epsilon(r)}{\epsilon^2}.$$

The extrema of $h'_\epsilon(r)$ are at $r = \pm\epsilon$, and thus

$$(6.6) \quad \|h'_\epsilon\|_\infty = \frac{1}{\epsilon} h_\epsilon(\epsilon) = \frac{e^{-\frac{1}{2}}}{\epsilon^2 \sqrt{2\pi}}.$$

If we estimate the integral $I_j := \int_{T_j} \varphi_x(y) dy = \int_{T_j} h_\epsilon(y-x) dy$ by

$$(6.7) \quad \hat{I}_j := h_\epsilon(y_j - x) \text{area } T_j,$$

where y_j is any point in T_j , (6.6) gives the error bound

$$E_j = |I_j - \hat{I}_j| \leq \delta_\epsilon \text{diam } T_j \text{area } T_j.$$

Now, for every polygonal domain Y , there exists an angle $\alpha \in (0, \pi)$, a constant $A > 0$, and a family of triangulations $\mathcal{T}_1, \mathcal{T}_2, \dots$ with $\mathcal{T}_N = \{T_{N,j}\}_{j=1}^N$ such that (i) the angles of every triangle in $\bigcup_{N \in \mathbb{N}} \mathcal{T}_N$ are bounded below by α ; and (ii) the maximum area of the triangles in \mathcal{T}_N are bounded above by A/N . By the triangle area formula, this means that there exists a constant c_α such that for all $N \in \mathbb{N}$ and $j \in \{1, \dots, N\}$,

$$\text{area } T_{N,j} \geq c_\alpha (\text{diam } T_{N,j})^2.$$

This leads to the following bound for the total error $\mathcal{E}_N := |I[\varphi_x] - I_N[\varphi_x]|$:

$$(6.8) \quad \begin{aligned} \mathcal{E}_N &\leq \sum_j E_j \leq \sum_{j=1}^N \delta_\epsilon \text{area}(T_j) \text{diam}(T_{N,j}) \leq \sum_{j=1}^N \delta_\epsilon c_\alpha^{-\frac{1}{2}} \text{area}(T_{N,j})^{\frac{3}{2}} \\ &\leq \delta_\epsilon c_\alpha^{-1/2} A^{3/2} N^{-1/2}. \end{aligned}$$

Thus, with such a triangulation, as $N \rightarrow \infty$ the error associated with the quadrature based on (6.7) converges to 0 at a rate $O(N^{-1/2})$ for piecewise-constant functions.

Let $\alpha_* \in (0, \pi)$ be the minimal edge angle over all vertices of the boundary of Y . Given an area parameter $a > 0$, the algorithm of [43] produces a triangulation

\mathcal{T}_{N_a} of Y with N_a elements such that (i) the minimal angle of every triangle in \mathcal{T}_{N_a} is at least α_* ; and (ii) the maximal area of the triangles in \mathcal{T}_N is no greater than a . In addition, under refinement of the triangulation, $a \mapsto a/k$ for $k \in \mathbb{N}$, the number of triangles increases linearly with k . This allows the convergence rate in (6.8) to be attained on a sequence $\mathcal{T}_{N_{a_1}}, \mathcal{T}_{N_{a_2}}, \dots$ with $a_k = a/k$. Faster rates of convergence can be obtained using higher-order quadrature schemes at the expense of a larger prefactor δ_ϵ associated with higher-order derivatives of h_ϵ . In this paper, we do not explore these options further as we found that the simple quadrature formula (6.7) gave satisfactory numerical results.

7. Applications to sea ice DEM data. We consider a time-evolving, finite collection of ice floes in a thick, bounded, open domain $\Omega \subset \mathbb{R}^2$. At any given time $t \in \mathbb{R}$, each floe is labeled by an index ℓ in a (finite) index set Λ_t and occupies a bounded, closed subset $S_{t,\ell} \subseteq \bar{\Omega}$. In addition, every ice floe has associated physical properties which are represented by continuous functions defined on $S_{t,\ell}$.

In what follows, we will be interested in mass density, velocity, and stress tensor fields, denoted as $m_{t,\ell} : S_{t,\ell} \rightarrow \mathbb{R}$, $\mathbf{v}_{t,\ell} : S_{t,\ell} \rightarrow \mathbb{R}^2$, and $\boldsymbol{\sigma}_{t,\ell} : S_{t,\ell} \rightarrow \mathbb{R}^{2 \times 2}$, respectively. We will denote a generic such function by $\tilde{f}_{t,\ell} : S_{t,\ell} \rightarrow \mathbb{R}^d$. At every time t , the floe-local functions $\tilde{f}_{t,\ell}$ collectively define a field $f_t : \Omega \rightarrow \mathbb{R}^d$ such that $f_t(x) = \sum_{\ell \in \Lambda_t} f_{t,\ell}$ where $f_{t,\ell} : \Omega \rightarrow \mathbb{R}^d$ is an extension of $\tilde{f}_{t,\ell}$ on the domain Ω defined as

$$(7.1) \quad f_{t,\ell}(x) = \begin{cases} \tilde{f}_{t,\ell}(x), & x \in S_{t,\ell}, \\ 0, & \text{otherwise.} \end{cases}$$

Note that f_t is a well-defined, piecewise-continuous function on Ω since Λ_t is a finite set and the floe-local functions $\tilde{f}_{t,\ell}$ are continuous. In particular, f_t is of the form (6.1) with f_ℓ in that equation set to the components of the \mathbb{R}^d -valued functions $\tilde{f}_{t,\ell}$. It should also be noted that the definition (6.1) allows for potential overlaps of the domains $S_{t,\ell}$, which may occur during floe–floe collisions.

Within this setup, we build a family of smooth approximations $g_{t,\epsilon,\mathbf{N}_t} : \Omega \rightarrow \mathbb{R}^d$ to f_t obtained by componentwise application of (6.2) followed by numerical approximation via triangulation method from subsection 6.3. Specifically, for a kernel lengthscale parameter ϵ and quadrature parameterized by the multi-index \mathbf{N}_t , we use (6.4) to obtain kernel-smoothed approximations of m_t , \mathbf{v}_t , and $\boldsymbol{\sigma}_t$, denoted by $m_{t,\epsilon,\mathbf{N}_t} : \Omega \rightarrow \mathbb{R}$, $\mathbf{v}_{t,\epsilon,\mathbf{N}_t} : \Omega \rightarrow \mathbb{R}^2$, and $\boldsymbol{\sigma}_{t,\epsilon,\mathbf{N}_t} : \Omega \rightarrow \mathbb{R}^{2 \times 2}$, respectively. Throughout, we employ the Gaussian RBF (2.1) as the kernel shape function h . The Gaussian RBF satisfies all of Properties (K1)–(K6) and the smoothed fields $m_{t,\epsilon,\mathbf{N}_t}$, $\mathbf{v}_{t,\epsilon,\mathbf{N}_t}$, and $\boldsymbol{\sigma}_{t,\epsilon,\mathbf{N}_t}$ are all infinitely differentiable.

7.1. Ice floe variables. The mass density, velocity field, and stress tensor field are employed in virtually all DEMs and continuum models of sea ice. In what follows, we describe their properties in a scenario where each ice floe is a spatially homogeneous object undergoing rigid body motion and experiencing point contact forces resulting from collisions with other ice floes and/or the domain boundaries. This scenario reflects how sea ice is modeled in the SubZero DEM [35] that we employ in our numerical experiments. Other modeling assumptions and/or physical variables can be handled by suitable modifications of the schemes described here.

Mass density field. Under our assumption of spatially homogeneous ice floes, the mass density function $m_{t,\ell}$ on each ice floe is constant; that is, we have $m_{t,\ell}(x) = \mu_{t,\ell}$ for all $x \in S_{t,\ell}$ where $\mu_{t,\ell}$. In the SubZero simulations analyzed in this paper, each ice floe has a fixed thickness $a_{t,\ell}$, and we have $\mu_{t,\ell} = \rho a_{t,\ell}$ where ρ is the (constant)

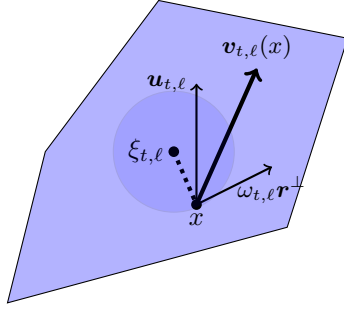


FIG. 3. Illustration of the center-of-mass velocity $\mathbf{u}_{t,\ell}$, rotational velocity $\omega_{t,\ell}\mathbf{r}^\perp$, and total velocity $\mathbf{v}_{t,\ell}$ at a point $x \in S_{t,\ell}$.

density of sea ice. Note that $a_{t,\ell}$ may undergo changes over time resulting from floe processes such as fracture and welding.

Velocity Field. Let $\xi_{t,\ell} \in \mathbb{R}^2$ be the center of mass for the floe $S_{t,\ell}$ and $\mathbf{u}_{t,\ell} \in \mathbb{R}^2$ the corresponding center-of-mass velocity. Under our assumption of rigid-body motion, the ice velocity $\mathbf{v}_{t,\ell}(x)$ at a point $x \in S_{t,\ell}$ is the sum of contributions from the center of mass velocity and rotational velocity; i.e., $\mathbf{v}_{t,\ell}(x) = \mathbf{u}_{t,\ell} + \omega_{t,\ell}\mathbf{r}^\perp$, where $\omega_{t,\ell}$ is the angular velocity (taken positive in the counter-clockwise sense), $\mathbf{r} = x - \xi_{t,\ell} \in \mathbb{R}^2$ is the displacement vector of x from the center of mass $\xi_{t,\ell}$, and $\mathbf{r}^\perp \in \mathbb{R}^2$ is the perpendicular vector to \mathbf{r} in the counter-clockwise sense. See Figure 3 for a schematic illustration.

Stress tensor field. The stress tensor field $\boldsymbol{\sigma}_{t,\ell}$ on each ice floe is a constant resulting from contact forces it experiences at any given time. Assuming that floe $S_{t,\ell}$ is subjected to contact forces $\mathbf{f}_{t,\ell,1}, \dots, \mathbf{f}_{t,\ell,M} \in \mathbb{R}^2$ acting at points $z_{t,\ell,1}, \dots, z_{t,\ell,M}$ on its boundary, the resulting stress tensor is given by

$$\boldsymbol{\sigma}_{t,\ell}(x) = \sum_{i=1}^M (\mathbf{r}_{t,\ell,i} \mathbf{f}_{t,\ell,i}^\top + \mathbf{f}_{t,\ell,i}^\top \mathbf{r}_{t,\ell,i}),$$

where $\mathbf{r}_{t,\ell,i} = z_{t,\ell,i} - \xi_{t,\ell}$ is the displacement vector of contact point $z_{t,\ell,i}$ from the center of mass $\xi_{t,\ell}$ and we treat $\mathbf{f}_{t,\ell,i}$ and $\mathbf{r}_{t,\ell,i}$ as column vectors.

7.2. SubZero simulations. We analyze two ice floe simulations performed using SubZero: (i) Nares Strait simulation; and (ii) lateral compression simulation. Results from these experiments are described in subsections 7.3 and 7.4, respectively.

In each case, the domain Ω is a subset of a square $\mathcal{S} \subset \mathbb{R}^2$ centered at the origin, whose sides have length 140 km. In the Nares Strait case, we build Ω by removing from \mathcal{S} points corresponding to the Canadian and Greenland land masses bounding the strait; see Figure 4. In the lateral compression case, Ω is the entire square \mathcal{S} .

Each SubZero run generates a time series of ice floes with domains $\{S_{t,\ell} \subseteq \Omega\}_{\ell \in \Lambda_t}$ and associated thickness $a_{t,\ell}$, center-of-mass velocity $\mathbf{u}_{t,\ell}$, angular velocity $\omega_{t,\ell}$, and contact forces $\mathbf{f}_{t,\ell,i}$. We sample these time series at a fixed time interval $\Delta t = Qt_+$, where Q is a positive integer and t_+ the simulation timestep. In our simulations we have $t_+ = 5$ s and $Q = 100$, leading to a sampling interval $\Delta t = 500$ s.

Using the sampled floe data, we compute associated mass, velocity, and stress tensor fields, $m_{t,\ell}$, $\mathbf{v}_{t,\ell}$, and $\boldsymbol{\sigma}_{t,\ell}$, respectively, as described in subsection 7.1. We then assemble these variables into piecewise-continuous mass density, velocity, and stress tensor fields, m_t , \mathbf{v}_t , and $\boldsymbol{\sigma}_t$, respectively, defined on Ω . For the computation of the

stress tensor, we aggregate the contact forces $\mathbf{f}_{t,\ell,i}$ on each ice floe over 100 timesteps, appropriately taking into account the floe’s fracture history. We smooth these fields using the Markov kernel (2.11) derived from the Gaussian RBF (2.1) with lengthscale parameter $\epsilon = 1.7$ km.

We numerically approximate the corresponding integral operator P_ϵ using the triangulation-based quadrature scheme described in subsection 6.1 with maximum triangle area of 0.5 km^2 . In our analyzed simulations, the number of ice floes at any time t varies (e.g., due to fracture) between 200 and 1300 and we take one quadrature point from each triangle. Applying the discretized integral operator leads to smooth density, velocity, and stress fields, which we denote here as $\hat{m}_t \equiv m_{t,\epsilon,N_t}$, $\hat{\mathbf{v}}_t \equiv \mathbf{v}_{t,\ell,N_t}$, and $\hat{\boldsymbol{\sigma}}_t \equiv \boldsymbol{\sigma}_{t,\ell,N_t}$, respectively. We evaluate the smooth fields on a collection of points $\{\mathbf{x}_i\} \subset \Omega$ given by the subset of the points in a 800×800 uniform grid of the bounding square \mathcal{S} that lie in Ω . The corresponding grid resolution is $140/800 \text{ km} = 175 \text{ m}$, but note that \hat{m}_t , $\hat{\mathbf{v}}_t$, and $\hat{\boldsymbol{\sigma}}_t$ are everywhere-defined smooth fields in Ω .

7.3. Nares Strait simulation. The Nares Strait is a narrow channel between Ellesmere Island in the Canadian Archipelago and Greenland that connects the Lincoln Sea of the Arctic Ocean to Baffin Bay in the Atlantic Ocean. Having a length of approximately 500 km and a minimum width of approximately 35 km, it plays an important role in transport between the Arctic and Atlantic Oceans, exhibiting complex sea ice dynamical phenomena such as jamming and arching that have been the focus of several modeling studies with both continuum models and DEMs [35, 52]. As our first experiment, we examine an idealized simulation of sea ice motion through a domain with a Nares Strait topography, visualized in Figure 4.

Ice floes of various shapes and sizes are initially placed in the domain Ω in a fully packed configuration. The floes are forced southward into the strait by quadratic drag induced from a constant southerly wind of velocity 10 m s^{-1} . In the ensuing simulation, (depicted in the left-hand column of Figure 4 at representative time instances with time increasing downwards) the floes experience a buildup of stress due to jamming. Eventually, floes begin to fracture, leading to a release of stress and decrease of average floe size that allows ice transport through the strait. In this simulation, floes are unbonded. Contact forces with the domain boundary are determined by numerically treating the coastlines as ice floes that are immovable but otherwise interact with other floes through unmodified contact forces.

The second, third, and fourth columns of Figure 4 from the left display scatterplots of the mass density field \hat{m}_t , the meridional (North–South) component of the velocity field $\hat{\mathbf{v}}_t$, and the trace of the tensor field $\hat{\boldsymbol{\sigma}}_t$. We use the latter to diagnose compressive stresses, which are associated with large negative values of $\text{tr } \hat{\boldsymbol{\sigma}}_t$. Examining the top row in Figure 4, we see that early on in the simulation the floes exhibit negligible meridional motion and are subjected to large compressive stresses induced by jamming and wind drag. At later times (second row) we see considerable reduction of stress in the southern half of the domain, as floes located there begin to fracture and move southward towards the exit of the strait. At late times (bottom row of Figure 4), we see additional buildup of southward velocity in the southern half of the domain as well as residual compressive stresses in the northern half due to jamming between unfractured floes.

7.4. Lateral compression simulation. In the second experiment, a lateral compression (i.e., compression directed along the y -axis) is applied to a square piece of ice of size $100 \text{ km} \times 100 \text{ km}$ located in the center of the $140 \text{ km} \times 140 \text{ km}$ domain Ω . The square ice piece consists of a collection of 200 ice floes of various shapes,

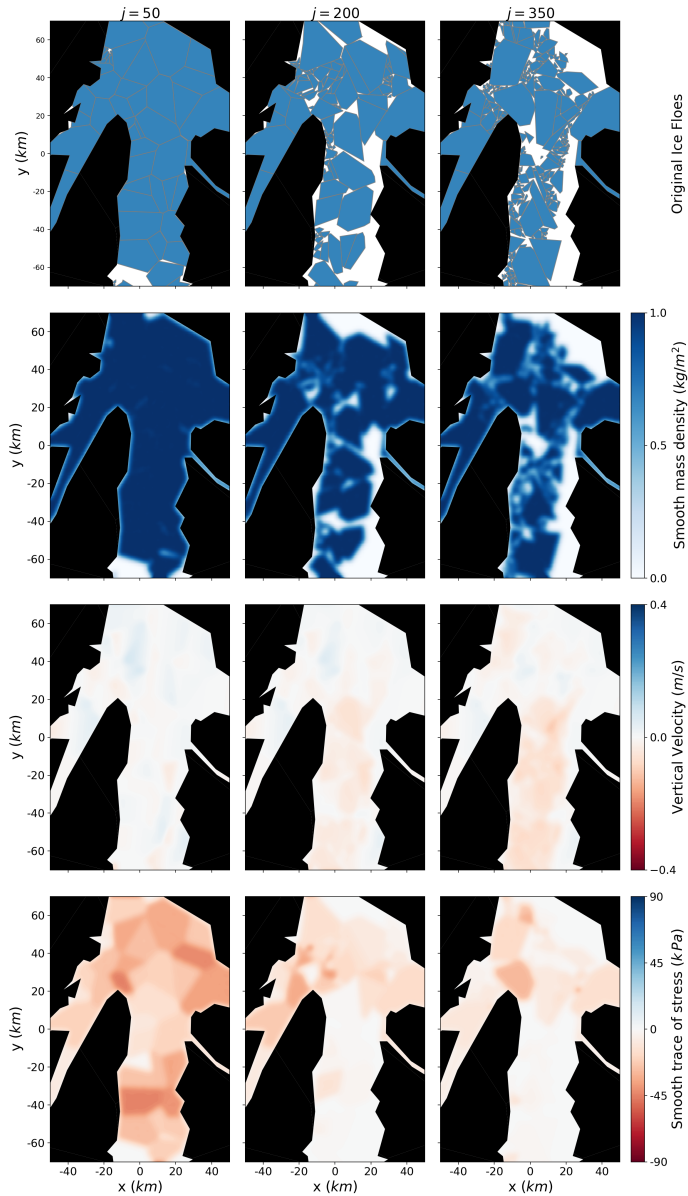


FIG. 4. Nares Strait simulation. The top row shows snapshots of the ice floes from the DEM at simulation times $t_j = j \Delta t$ with $j = 50$ (left), 200 (center), and 350 (right). The second, third, and fourth rows from the top show snapshots of kernel-smoothed mass density \hat{m}_t , meridional velocity (y component of $\hat{\mathbf{v}}_t$), and trace of the stress field $\text{tr} \hat{\boldsymbol{\sigma}}_t$, respectively, at the times t_j .

arranged in a densely packed configuration. Unlike the Nares Strait case, ice floes in this example are bonded. Numerically, the bonds are implemented as small-sized ice floes of a “bow-tie” shape, which are inserted randomly in the boundaries between floes. The north/south boundaries move at a constant prescribed velocity of 0.1 m s^{-1} toward the center. The atmospheric and oceanic stresses are set to zero in this simulation. As stress builds up due to the externally imposed lateral stress, the bow-tie

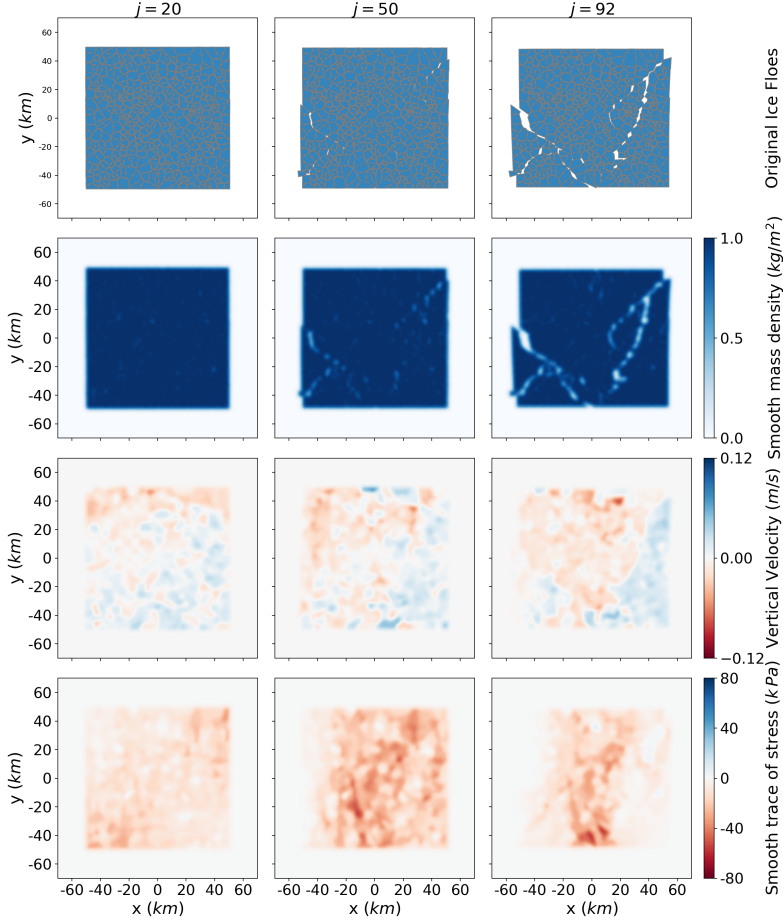


FIG. 5. As in Figure 4, but for the lateral compression experiment. The time instances $t_j = j \Delta t$ shown are for $j = 20$ (left), 50 (center), and 92 (right).

floes can fracture under spatially-uniform fracture criteria, allowing the floes to move in directions transverse to the applied pressure. The resulting dynamical evolution exhibits fracture patterns with long-range correlations resembling LKFs. See the top row of Figure 5 for a visualization of the simulation at representative time instances.

The second, third, and fourth rows of Figure 5 from the top show scatterplots of the kernel-smoothed mass density \hat{n}_t , the y component of velocity \hat{v}_t , and trace of the stress tensor $\hat{\sigma}_t$ in a similar manner as Figure 4. Early on in the simulation (left column), the stress field exhibits a fairly diffuse compressive pattern in space as the floes are tightly packed and bonds as unbroken. As bonds start to break (center and right columns), we see that stress becomes increasingly concentrated in a wedge-shaped region of high ice concentration that connects the lateral domain boundaries where stress is applied. Meanwhile, chunks of ice adjacent to the central wedge-shape region move sideways, leading to a noticeable pattern in the velocity field component. As with the Nares Strait simulation, the smoothed stress tensor field $\hat{\sigma}_t$ reveals stress patterns that are not readily noticeable in the raw DEM contact forces.

8. Conclusions. In this paper, we studied the convergence properties of one-parameter families of integral operators with Markovian kernels constructed from normalization of convolution operators associated with radial kernel functions. Using the theory of Hardy–Littlewood maximal operators in conjunction with a thickness condition that bounds the Lebesgue density of the spatial domain Ω from below, we proved pointwise and L^p norm convergence results for continuous approximations of $f \in L^p(\Omega)$, $p \in (1, \infty)$, by $P_\epsilon f$ for Markov operators P_ϵ obtained by left normalization of integrable radial kernels with lengthscale parameter ϵ (Theorem 2.8). We also showed L^p norm convergence for approximations $\tilde{P}_\epsilon f$ obtained from Markov operators with bistochastic kernels (Theorem 5.1) that preserve integrals of functions in addition to preserving constant functions. The paper also studied properties of thick sets from the perspective of metric measure spaces, where it was shown that thickness implies a locally doubling condition on Ω but is in general independent from (global) doubling (Propositions 4.1 and 4.2).

Numerically, our approach can be implemented using a variety of quadrature schemes, including Monte Carlo and mesh-based schemes. Here, we have focused on a deterministic quadrature scheme based on triangulation of polygonal domains. Using this approach, we built smooth approximations of piecewise-continuous mass density, velocity, and stress tensor fields from discrete element models (DEMs) of sea ice dynamics. We used the smoothed fields to characterize stress patterns associated with jamming and fracture of wind-forced floes passing through the Nares Strait and the formation of idealized linear kinematic features resulting from lateral compression. These results demonstrate the utility of kernel smoothing for postprocessing and retrieval of physically meaningful information from DEM simulations.

Throughout this work, the Lebesgue measure on \mathbb{R}^n played a central role by providing the background measure for Markov normalization. A possible avenue of future work would be to study the convergence properties of Markov operators built from measures other than Lebesgue, such as invariant measures of dynamical systems. From the point of view of applications, it would be fruitful to explore use-cases of the reconstructed smooth fields to infer macro-scale constitutive laws emerging from DEM simulations, along with associated rheology parameterization schemes.

Appendix A. Proofs of auxiliary results.

Proof of Lemma 2.1. For every $q \in [1, \infty)$, the group of translation operators $\{T_x : L(\mathbb{R}^n) \rightarrow L(\mathbb{R}^n)\}_{x \in \mathbb{R}^n}$ extends to a strongly continuous group on $L^q(\mathbb{R}^n)$ that acts by isometries; that is, the mapping $x \mapsto T_x h \in L^q(\mathbb{R}^n)$ is norm-continuous at every $x \in \mathbb{R}^n$ for every $h \in L^q(\mathbb{R}^n)$ and $\|T_x h\|_{L^q(\mathbb{R}^n)} = 1$. Since $L^p(\mathbb{R}^n) \simeq L^{q^*}(\mathbb{R}^n)$, $\varphi : h \mapsto \int_{\mathbb{R}^n} f(y)h(y) dy$ is a bounded functional on $L^q(\mathbb{R}^n)$. Moreover, for every $x \in \mathbb{R}^n$ we have $f * h(x) = \varphi((T_x h)^\vee)$. The continuity of $h * f$ follows from the facts that φ and $^\vee$ are continuous maps on $L^q(\mathbb{R}^n)$ and $\{T_x : L^q(\mathbb{R}^n) \rightarrow L^q(\mathbb{R}^n)\}_{x \in \mathbb{R}^n}$ is strongly continuous. The bound $\|h * f\|_\infty \leq \|h\|_{L^q(\mathbb{R}^n)} \|f\|_{L^p(\mathbb{R}^n)}$ follows from Hölder’s inequality and the fact that T_x acts on $L^q(\mathbb{R}^n)$ as an isometry. \square

Proof of Lemma 2.2. By a change of variables, it is enough to prove the claim for $\epsilon = 1$.

Starting from the $r = 1$ case, let $e_1, \dots, e_n \in \mathbb{R}^n$ be the standard basis vectors of \mathbb{R}^n and $D_j : E_j \rightarrow \mathbb{L}^2(\mathbb{R}^n)$ the generators of the (unitary) translation group on $L^2(\mathbb{R}^n)$ along e_j . That is, D_j is a skew-adjoint operator defined on a dense subspace $E_j \subset L^2(\mathbb{R}^n)$ by the $L^2(\mathbb{R}^n)$ -norm limit $D_j h = \lim_{s \rightarrow 0} (T_{se_j} h - h)/s$. Let $\hat{E}_j = \{\hat{h} \in L^2(\mathbb{R}^n) : \int_{\mathbb{R}^n} \omega_j^2 |\hat{h}(\omega)|^2 d\omega < \infty\}$. The generators D_j map under the unitary Fourier

transform $\mathcal{F} : L^2(\mathbb{R}^n) \rightarrow L^2(\mathbb{R}^n)$ to the multiplication operators $\hat{D}_j : \hat{E}_j \rightarrow L^2(\mathbb{R}^n)$ where $\hat{D}_j = \mathcal{F}^* D_j \mathcal{F}$ and $\hat{D}_j \hat{h}(\omega) = i\omega_j \hat{h}(\omega)$. For $h \in H^1(\mathbb{R}^n)$ we have that $\omega \mapsto i\omega_j \hat{h}(\omega) \in L^2(\mathbb{R}^n)$ since $\omega \mapsto (1 + \|\omega\|^2)^{1/2} \hat{h}(\omega) \in L^2(\mathbb{R}^n)$ and $|\omega_j| \leq C(1 + \|\omega\|^2)^{1/2}$ for a constant C . As a result, h lies in E_j . By properties of one-parameter unitary groups (e.g., [42, Proposition 6.5]), the function $u(t) = T_{te_j} h$ lies in $C^1(\mathbb{R}, L^2(\mathbb{R}^n))$; that is, $u'(t) = \lim_{s \rightarrow 0} (T_{(t+s)e_j} h - T_{te_j} h)/s$ is well-defined and continuous at every $t \in \mathbb{R}$. As a result, for every $f \in L^2(\mathbb{R}^n)$ and $x \in \mathbb{R}^n$, the function $t \mapsto \varphi((T_{te_j} h)^\vee)$ with $\varphi h = \int_{\mathbb{R}^n} f(y) h(y) dy$ lies in $C^1(\mathbb{R})$. Writing $x = \sum_{j=1}^n x_j e_j$ with $x_j \in \mathbb{R}$, we conclude that $x \mapsto \varphi((T_x h)^\vee) = \varphi((T_{x_1 e_1} \circ \dots \circ T_{x_n e_n} h)^\vee)$ lies in $C^1(\mathbb{R}^n)$.

Next, for $r \geq 1$, we have $(1 + \|\omega\|^2)^{r/2} \geq C|\omega_j|(1 + \|\omega\|^2)^{(r-1)/2}$ which implies that $D_j h \in H^{r-1}(\mathbb{R}^n)$ whenever $h \in H^r(\mathbb{R}^n)$. Using this fact, we show by induction that $u(t) = T_{te_j} h$ lies in $C^r(\mathbb{R}, L^2(\mathbb{R}^n))$; recursively, this means that $u'(t) = \lim_{s \rightarrow 0} (T_{(t+s)e_j} h - T_{te_j} h)/s$ lies in $C^{r-1}(\mathbb{R}, L^2(\mathbb{R}^n))$. We have already proved the base case, $r = 1$, so suppose that for $r - 1 \in \mathbb{N}_0$ it holds that for every $g \in H^{r-1}(\mathbb{R}^n)$, $w(t) = T_{te_j} g$ lies in $C^{r-1}(\mathbb{R}, L^2(\mathbb{R}^n))$. In that case, for $h \in H^r(\mathbb{R}^n)$ and $u(t) = T_{te_j} h$ we have $u'(t) = D_j T_{te_j} h = T_{te_j} D_j h = T_{te_j} g$ with $g = D_j h \in H^{r-1}(\mathbb{R}^n)$. We therefore deduce that $u' \in C^{r-1}(\mathbb{R}, L^2(\mathbb{R}^n))$ and thus that $u \in C^r(\mathbb{R}, L^2(\mathbb{R}^n))$. With this result and $f \in L^2(\mathbb{R}^n)$, $\varphi \in L^{2^*}(\mathbb{R}^n)$, and $x = \sum_{j=1}^n x_j e_j$ as above, it follows that $t \mapsto \varphi((T_{te_j} h)^\vee)$ lies in $C^r(\mathbb{R})$ and $x \mapsto \varphi((T_x h)^\vee) = \varphi((T_{x_1 e_1} \circ \dots \circ T_{x_n e_n} h)^\vee)$ lies in $C^r(\mathbb{R}^n, \mathbb{R})$. \square

Proof of Lemma 5.2. Let A be an upper bound for $\|f\|_{L^\infty(\Omega)}$ and $\|f_\epsilon\|_{L^\infty(\Omega)}$ and fix $g \in L^p(\Omega)$. For every $\delta > 0$, there exists $\tilde{g} \in C_c(\Omega)$ such that $\|g - \tilde{g}\|_{L^p(\Omega)} < \delta$. We have

$$\begin{aligned} \|M_{f_\epsilon} g - M_f g\|_{L^p(\Omega)} &= \|(f_\epsilon - f)g\|_{L^p(\Omega)} \\ &\leq \|(f_\epsilon - f)(g - \tilde{g})\|_{L^p(\Omega)} + \|(f_\epsilon - f)\tilde{g}\|_{L^p(\Omega)} \\ &\leq \|f_\epsilon - f\|_{L^p(\Omega)} \delta + \|f_\epsilon - f\|_{L^p(\Omega)} \|\tilde{g}\|_\infty \\ &\leq 2A\delta + \|f_\epsilon - f\|_{L^p(\Omega)} \|\tilde{g}\|_\infty. \end{aligned}$$

The claim follows from the fact that δ was arbitrary and $\lim_{\epsilon \rightarrow 0} \|f_\epsilon - f\|_{L^p(\Omega)} = 0$. \square

REFERENCES

- [1] D. BELTRAN, J. P. G. RAMOS, AND O. SAARI, *Regularity of fractional maximal functions through Fourier multipliers*, J. Funct. Anal., 276 (2019), pp. 1875–1892, <https://doi.org/10.1016/j.jfa.2018.11.004>.
- [2] T. BERRY AND T. SAUER, *Local kernels and the geometric structure of data*, Appl. Comput. Harmon. Anal., 40 (2016), pp. 439–469, <https://doi.org/10.1016/j.acha.2015.03.002>.
- [3] E. BLOCKLEY ET AL., *The future of sea ice modeling: Where do we go from here?*, Bull. Amer. Meteor. Soc., 101 (2020), pp. E1304–E1311, <https://doi.org/10.1175/BAMS-D-20-0073.1>.
- [4] R. E. CAFLISCH, *Monte carlo and quasi-Monte Carlo methods*, Acta Numer., 7 (1998), pp. 1–49, <https://doi.org/10.1017/S0962492900002804>.
- [5] E. CARNEIRO AND C. GONZÁLEZ-RIQUELME, *Gradient bounds for radial maximal functions*, Ann. Fenn. Math., 46 (2021), pp. 495–521, <https://doi.org/10.5186/aasfm.2021.4631>.
- [6] E. CARNEIRO AND B. F. SVAITER, *On the variation of maximal operators of convolution type*, J. Funct. Anal., 265 (2013), pp. 837–865, <https://doi.org/https://doi.org/10.1016/j.jfa.2013.05.012>.
- [7] N. CHEN, S. FU, AND G. E. MANUCHARYAN, *An efficient and statistically accurate Lagrangian data assimilation algorithm with applications to discrete element sea ice models*, J. Comput. Phys., 455 (2022), <https://doi.org/10.1016/j.jcp.2022.111000>.
- [8] F. R. K. CHUNG, *Spectral Graph Theory*, vol. 97 of CBMS Regional Conference Series in Mathematics, American Mathematical Society, Providence, 1997.

- [9] R. COIFMAN AND M. HIRN, *Bi-stochastic kernels via asymmetric affinity functions*, Appl. Comput. Harmon. Anal., 35 (2013), pp. 177–180, <https://doi.org/10.1016/j.acha.2013.01.001>.
- [10] M. D. COON, R. KWOK, M. PRUIS, G. LEVY, D. SULSKY, AND H. L. SCHREYER, *Arctic Ice Dynamics Joint Experiment (AIDJEX) assumptions revisited and found inadequate*, J. Geophys. Res., 112 (2007), C11S90, <https://doi.org/10.1029/2005JC003393>.
- [11] A. DAMSGAARD, A. ADCROFT, AND O. SERGIENKO, *Application of discrete element methods to approximate sea ice dynamics*, J. Adv. Model. Earth Syst., 10 (2018), pp. 2228–2244, <https://doi.org/10.1029/2018MS001299>.
- [12] V. DANSEREAU, J. WEISS, P. SARAMITO, AND P. LATTER, *A Maxwell-elasto-brittle rheology for sea ice modelling*, Cryosphere, 10 (2016), pp. 1339–1359, <https://doi.org/https://doi.org/10.5194/TC-10-1339-2016>.
- [13] S. DAS, D. GIANNAKIS, AND J. SLAWINSKA, *Reproducing kernel Hilbert space compactification of unitary evolution groups*, Appl. Comput. Harmon. Anal., 54 (2021), pp. 75–136, <https://doi.org/10.1016/j.acha.2021.02.004>.
- [14] B. N. DI, Q. J. HE, AND D. Y. YAN, *Two-weight norm inequalities for local fractional integrals on Gaussian measure spaces*, Acta Math. Sin. Engl., 38 (2022), p. 1203–1228, <https://doi.org/10.1007/s10114-022-1114-6>.
- [15] L. EVANS, *Partial Differential Equations*, Graduate Studies in Mathematics, American Mathematical Society, 2022, <https://books.google.com/books?id=Ott1EAAAQBAJ>.
- [16] D. L. FELTHAM, *Sea ice rheology*, Annu. Rev. Fluid Mech., 40 (2008), pp. 91–112, <https://doi.org/10.1146/annurev.fluid.40.111406.102151>.
- [17] R. GIBARA AND J. KLINE, *Fractional maximal functions and mean oscillation on bounded doubling metric measure spaces*, J. Funct. Anal., 285 (2023), 110126, <https://doi.org/10.1016/j.jfa.2023.110126>.
- [18] C. GONZÁLEZ-RIQUELME, *On the continuity of maximal operators of convolution type at the derivative level*, Isr. J. Math., 253 (2021), pp. 745–759, <https://doi.org/10.1007/s11856-022-2375-6>.
- [19] M. GUPTA AND A. F. THOMPSON, *Regimes of sea-ice floe melt: Ice–ocean coupling at the submesoscales*, J. Geophys. Res. Oceans, 127 (2022), e2022JC018894, <https://doi.org/10.1029/2022JC018894>.
- [20] T. HEIKKINEN, J. KINNUNEN, J. KORVENPAA, AND H. TUOMINEN, *Regularity of the local fractional maximal function*, Ark. Mat., 53 (2015), pp. 127–154, <https://doi.org/10.1007/s11512-014-0199-2>.
- [21] J. HEINONEN, *Lectures on Analysis on Metric Spaces*, Universitext, Springer, New York, 2001.
- [22] A. HERMAN, *Discrete-element bonded-particle Sea Ice model DESIgn, version 1.3a—model description and implementation*, Geosci. Model Dev., 9 (2016), pp. 1219–1241, <https://doi.org/10.5194/gmd-9-1219-2016>.
- [23] A. HERMAN, *Wave-induced stress and breaking of sea ice in a coupled hydrodynamic discrete-element wave–ice model*, Cryosphere, 11 (2017), pp. 2711–2725, <https://doi.org/10.5194/tc-11-2711-2017>.
- [24] A. HERMAN, *Granular effects in sea ice rheology in the marginal ice zone*, Phil. Trans. R. Soc. A, 380 (2022), 20210260, <https://doi.org/10.1098/rsta.2021.0260>.
- [25] W. D. I. HIBLER, *A dynamic thermodynamic sea ice model*, J. Phys. Oceanogr., 9 (1979), pp. 815–846, [https://doi.org/10.1175/1520-0485\(1979\)009<0815:ADTSIM>2.0.CO;2](https://doi.org/10.1175/1520-0485(1979)009<0815:ADTSIM>2.0.CO;2).
- [26] M. A. HOPKINS, *On the mesoscale interaction of lead ice and floes*, J. Geophys. Res., 101 (1996), pp. 18315–18326, <https://doi.org/10.1029/96JC01689>.
- [27] E. C. HUNKE AND J. K. DUKOWICZ, *An elastic–viscous–plastic model for sea ice dynamics*, J. Phys. Oceanogr., 27 (1997), pp. 1849–1867, [https://doi.org/10.1175/1520-0485\(1997\)027<1849:AEVPMF>2.0.CO;2](https://doi.org/10.1175/1520-0485(1997)027<1849:AEVPMF>2.0.CO;2).
- [28] J. K. HUTCHINGS, *Modeling linear kinematic features in sea ice*, Mon. Weather Rev., 133 (2005), pp. 3481–3497, <https://doi.org/10.1175/MWR3045.1>.
- [29] J. KINNUNEN, *The Hardy–Littlewood maximal function of a Sobolev function*, Isr. J. Math., 100 (1997), pp. 117–124, <https://doi.org/10.1007/BF02773636>.
- [30] J. KINNUNEN AND P. LINDQVIST, *The derivative of the maximal function*, Journal Fur Die Reine Und Angewandte Mathematik - J REINE ANGEW MATH, 1998 (1998), pp. 161–167, <https://doi.org/10.1515/crll.1998.095>.
- [31] M. KREYSCHER, M. HARDER, P. LEMKE, AND G. M. FLATO, *Results of the Sea Ice Model Inter-comparison Project: Evaluation of sea ice rheology schemes for use in climate simulations*, J. Geophys. Res., 105 (2000), pp. 11299–11320, <https://doi.org/10.1029/1999JC000016>.
- [32] R. KWOK, *Deformation of the Arctic Ocean sea ice cover between November 1996 and April 1997: A qualitative survey*, in IUTAM Symposium on Scaling Laws in Ice Mechanics and Ice Dynamics, J. P. Dempsey and H. H. Shen, eds., Kluwer Academic Publishers, 2001,

- pp. 315–322.
- [33] A. K. LERNER, *An elementary approach to several results on the Hardy–Littlewood maximal operator*, Proc. Amer. Math. Soc., 136 (2008), pp. 2829–2833, <https://www.jstor.org/stable/20535485>.
 - [34] F. LIU, H. WU, Q. XUE, AND K. YABUTA, *Endpoint Sobolev boundedness and continuity of multilinear fractional maximal functions*, Bull. Sci. Math., 179 (2022), 103155, <https://doi.org/https://doi.org/10.1016/j.bulsci.2022.103155>.
 - [35] G. E. MANUCHARYAN AND B. P. MONTEMURO, *SubZero: A Sea ice model with an explicit parameterization of a floe life cycle.*, J. Adv. Model. Earth Syst., 14 (2022), e2022MS003247, <https://doi.org/10.1029/2022MS003247>.
 - [36] G. E. MANUCHARYAN AND A. F. THOMPSON, *Heavy footprints of upper-ocean eddies on weakened Arctic seaice in marginal ice zones*, Nat. Commun., 13 (2022), 2147, <https://doi.org/10.1038/s41467-022-29663-0>.
 - [37] R. MONCARDA, M. GUPTA, A. THOMPSON, AND J. E. ANDRADE, *Level Set Discrete Element Method for modeling sea ice floes*, Comput. Methods. Appl. Mech. Eng., 406 (2023), 115891, <https://doi.org/10.1016/j.cma.2023.115891>.
 - [38] Y. PAN AND Q. XUE, *Two weight characterizations for the multilinear local maximal operators*, Acta Math. Sci., 41 (2021), pp. 596–608, <https://doi.org/10.1007/s10473-021-0219-9>.
 - [39] M. RABATEL, S. LABBÉ, AND J. WEISS, *Dynamics of an assembly of rigid ice floes*, J. Geophys. Res. Oceans, 120 (2015), pp. 5887–5909, <https://doi.org/10.1002/2015JC010909>.
 - [40] M. RAMSEYER, O. SALINAS, AND M. TOSCHI, *Two-weight boundedness for local fractional maximal and applications*, Eur. J. Math., 9 (2023), 109, <https://doi.org/10.1007/s40879-023-00708-y>.
 - [41] J. RUPPERT, *A Delaunay refinement algorithm for quality 2-dimensional mesh generation*, J. Algorithm., 18 (1995), pp. 5480–585, <https://doi.org/10.1006/jagm.1995.1021>.
 - [42] K. SCHMÜDGEN, *Unbounded Self-Adjoint Operators on Hilbert Space*, vol. 265 of Graduate Texts in Mathematics, Springer Science+Business Media, 2012.
 - [43] J. R. SHEWCHUK, *Delaunay refinement algorithms for triangular mesh generation*, Comput. Geom., 22 (2002), pp. 21–74, [https://doi.org/10.1016/S0925-7721\(01\)00047-5](https://doi.org/10.1016/S0925-7721(01)00047-5).
 - [44] M. SHI AND J. ZHOU, *Some estimates of operators on local mixed Morrey-type spaces*, Indian J. Pure Appl. Math., (2023), <https://doi.org/10.1007/s13226-023-00432-z>.
 - [45] Y.-H. SHIH, C. MEHLMANN, M. LOSCH, AND G. STADLER, *Robust and efficient primal-dual Newton-Krylov solvers for viscous-plastic sea-ice models*, J. Comput. Phys., 474 (2023), 111802, <https://doi.org/10.1016/j.jcp.2022.111802>.
 - [46] E. M. STEIN, *Harmonic Analysis: Real-Variable Methods, Orthogonality, and Oscillatory Integrals*, vol. 43 of Princeton Mathematical Series, Princeton University Press, Princeton, 1993.
 - [47] K. STEMPAK, *Modified Hardy–Littlewood maximal operators on nondoubling metric measure spaces*, Ann. Acad. Sci. Fenn. Math., 40 (2015), pp. 443–448, <https://doi.org/10.5186/aasfm.2015.4024>.
 - [48] K. STEMPAK AND X. TAO, *Local Morrey and Campanato spaces on quasimetric measure spaces*, J. Funct. Spaces., 2014 (2014), 172486, <https://doi.org/10.1155/2014/172486>.
 - [49] J. TUKHURI AND A. POLOJÄRVI, *A review of discrete element simulation of ice–structure interaction*, Phil. Trans. R. Soc. A, 376 (2018), 20170335, <https://doi.org/10.1098/rsta.2017.0335>.
 - [50] P. VIOLA AND B. VIVIANI, *Local maximal functions and operators associated to Laguerre expansions*, Tohoku Math. J., 66 (2014), pp. 155 – 169, <https://doi.org/10.2748/tmj/1404911859>.
 - [51] J. WEIGT, *Endpoint Sobolev bounds for fractional Hardy–Littlewood maximal operators*, Math. Z., 301 (2022), pp. 2317–2337, <https://doi.org/10.1007/s00209-022-02969-x>.
 - [52] B. WEST, D. O’CONNOR, M. PARNO, M. KRACKOW, AND C. POLASHENSKI, *Bonded discrete element simulations of sea ice with non-local failure: Applications to Nares Strait*, J. Adv. Model. Earth Syst., 14 (2022), e2021MS002614, <https://doi.org/10.1029/2021MS002614>.
 - [53] J. ZHANG, *Sea ice properties in high-resolution sea ice models*, J. Geophys. Res. Oceans, 126 (2021), e2020JC016686, <https://doi.org/10.1029/2020JC016686>.
 - [54] Y. ZHENG AND Y. MING, *Low-level cloud budgets across sea ice edges*, J. Climate, 36 (2023), pp. 3–18, <https://doi.org/10.1175/JCLI-D-22-0301.1>.